Structural and functional properties of the transporter SLC26A6 reveal mechanism of coupled anion exchange

David N. Tippett[1], Colum Breen[2], Stephen J. Butler[2], Marta Sawicka[1] and Raimund Dutzler[1*]

[1]Department of Biochemistry, University of Zurich, Zurich, Switzerland

[2]Department of Chemistry, Loughborough University, Loughborough, UK

*For correspondence: dutzler@bioc.uzh.ch (RD)

Abstract

Members of the SLC26 family constitute a conserved family of anion transport proteins, which encompasses uncoupled transporters with channel-like properties, coupled exchangers and motor proteins. Among the eleven paralogs in humans, several participate in the secretion of bicarbonate in exchange with chloride and thus play an important role in pH homeostasis. Previously, we have elucidated the structure of murine SLC26A9 and defined its function as an uncoupled chloride transporter (Walter, Sawicka, & Dutzler, 2019). Here we have determined the structure of the closely related human transporter SLC26A6 and characterized it as a strictly coupled exchanger of chloride with either bicarbonate or oxalate. The structure defines an inward-facing conformation of the protein that generally resembles known structures of SLC26A9. The altered anion selectivity between both paralogs is a consequence of a remodeled ion binding site located in the center of a mobile unit of the membrane-inserted domain, which also accounts for differences in the coupling mechanism.

Introduction

Bicarbonate (HCO_3^-), the conjugate base of carbonic acid, is a waste product of the citric acid cycle and an important buffer in the intra- and extracellular environment. Its transport across cellular membranes thus constitutes an important mechanism for the control of intracellular pH and the increased buffer capacity of bodily fluids and secretions (Alka & Casey, 2014). This process is mediated by distinct channels and secondary transporters, the latter comprising paralogs of the SLC4 and SLC26 families. The SLC26 transporters constitute an abundant class of anion transport proteins that are expressed in all kingdoms of life with a considerable degree of sequence conservation (Alper & Sharma, 2013; Dorwart, Shcheynikov, Yang, & Muallem, 2008). Whereas homologs in prokaryotes and plants were classified as symporters, where the uptake of mono- and divalent anions is coupled to the import of either sodium ions or protons (Geertsma et al., 2015; C. Wang et al., 2019; L. Wang, Chen, & Zhou, 2021), the transporters in animals show mechanistic differences. Among the ten functional SLC26 paralogs in humans, we find an astonishing mechanistic breadth. Family members function as either coupled anion exchangers, anion transporters with channel-like properties and in the case of SLC26A5 (Prestin), as a motor protein in cochlear outer hair cells (Alper & Sharma, 2013). Among the paralogs which have retained their transport function, the distinction between coupled and uncoupled transporters is most pronounced. Whereas most family members operate as exchangers of different anions including the monovalent ions chloride (Cl^-), bicarbonate (HCO_3^-), iodide and formate and the divalent ions sulfate and oxalate (Alper & Sharma, 2013), the protein SLC26A9 functions as fast passive transporter of Cl^- (Dorwart, Shcheynikov, Wang, Stippec, & Muallem, 2007; Walter et al., 2019). Our previous study has characterized the structural and functional properties of the murine paralog of SLC26A9 (Walter et al., 2019). The protein adopts a homodimeric architecture that is

45 representative for the entire SLC26 family. Each subunit consists of a membrane inserted transport
46 domain (TM) followed by a cytoplasmic STAS domain, which together with the extended N-
47 terminus mediates the bulk of the subunit interactions with few contacts in the membrane-inserted
48 region (Walter et al., 2019). The TMs share an architecture that was initially identified in the
49 prokaryotic transporter UraA (Lu et al., 2011), and that was later defined in the prokaryotic
50 homologue SLC26Dg as common framework for the entire family (Geertsma et al., 2015). In this
51 architecture, the TM segregates into two separate motifs that adopt distinct roles during transport,
52 respectively termed 'core' and 'gate' domains. The gate domain forms a contiguous rigid scaffold
53 with the cytosolic STAS domain that remains static during transport. Conversely the mobile core
54 domain harbors a selective anion binding site and acts as mobile unit during the transport cycle.
55 The core domain alternately exposes the substrate site to different sides of the membrane as
56 expected for a protein working by an elevator-type transport mechanism (Drew & Boudker, 2016;
57 Walter et al., 2019). Despite its classification as membrane transporter, SLC26A9 mediates large
58 channel-like chloride currents that saturate at high mM concentration and it efficiently
59 discriminates against HCO_3^- (Dorwart et al., 2007; Walter et al., 2019). Its function as a fast
60 electrogenic chloride transporter and selection against HCO_3^- is astonishing since several other
61 family members have been classified as Cl^-/ HCO_3^- exchangers (Alper & Sharma, 2013). One of
62 the family members sharing this property is the protein SLC26A6 (Knauf et al., 2001; Lohi et al.,
63 2000). SLC26A6 is widely expressed in different tissues including the heart, kidney, pancreas and
64 intestine (J. Wang, Wang, Wang, & Tuo, 2020). Besides its function as HCO_3^- transporter, it also
65 plays an important role in the extrusion of oxalate to prevent the formation of kidney stones (Clark
66 et al., 2008; Jiang et al., 2006; Ohana, Shcheynikov, Moe, & Muallem, 2013). Similar to
67 SLC26A9, the protein acts in synergy with the chloride channel CFTR and was proposed to engage

68 in direct interaction and mutual regulation (Bertrand et al., 2017; Dorwart et al., 2008;
69 Shcheynikov, Ko, et al., 2006; Y. Wang et al., 2006). The stoichiometry of HCO_3^- and oxalate
70 transport by SLC26 is still controversial, as transport of both ions has been described in different
71 studies as either electrogenic or electroneutral (Chernova et al., 2005; Clark et al., 2008; Kim,
72 Myers, Sihn, Rafizadeh, & Zhang, 2013; Ohana, Yang, Shcheynikov, & Muallem, 2009;
73 Shcheynikov, Wang, et al., 2006; Xie, Welch, Mercado, Romero, & Mount, 2002). This question
74 is particularly pertinent in light of the divergent net charge of both substrates, with HCO_3^- being
75 monovalent and oxalate divalent under physiological conditions. Consequently, the structural
76 basis for the mechanistic distinction between the uncoupled SLC26A9 and the coupled SLC26A6
77 and the basis for their pronounced selectivity, with Cl^- acting as common substrate of both proteins,
78 has remained elusive.
79 To address these open questions, we here present a thorough structural and functional
80 characterization of the human transporter SLC26A6 combining cryo-electron microscopy with
81 electrophysiology and liposomal transport assays. With respect to its overall structure, SLC26A6
82 closely resembles its paralog SLC26A9 although it shows a distinct transport mechanism. The
83 protein mediates electroneutral Cl^-/ HCO_3^- and electrogenic Cl^-/oxalate exchange, which is in stark
84 contrast to the uncoupled Cl^- transport of SLC26A9 and which is accomplished by an altered ion
85 binding site located in the mobile core domain of the transmembrane transport unit.
86
87 **Results**
88
89 **Functional characterization of SLC26A6**

90 We have previously characterized the transport properties of murine SLC26A9 by patch clamp
91 electrophysiology and found comparably large and selective Cl^- currents. SLC26A9 currents were
92 shown to reverse at the Nernst potential of the conducting anion, which distinguishes the protein
93 as an uncoupled chloride transporter (Walter et al., 2019) (Figure 1A, Figure 1-Figure Supplement
94 1A). The high magnitude of these ohmic currents, which lack any time-dependence in response to
95 voltage changes, originate from an unusually active protein that transports anions with channel-
96 like properties (Figure 1-Figure Supplement 1A). SLC26A9 shows a lyotropic permeability
97 sequence that facilitates the transport of Cl^-, isothiocyanate, I^- and nitrate but not sulfate or HCO_3^-
98 (Walter et al., 2019) (Figure 1A, Figure 1-Figure Supplement 1A). The inability to conduct HCO_3^-
99 is an exception in a family where most members work as transporters of this abundant anion (Alper
100 & Sharma, 2013; Ohana et al., 2009). To investigate mechanistic differences between this passive
101 Cl^- transporter and its paralogs functioning as coupled antiporters, we have turned our attention
102 towards the protein SLC26A6, which was proposed to mediate electrogenic Cl^-/HCO_3^- exchange
103 (Ohana et al., 2009; Shcheynikov, Wang, et al., 2006). Hence, we initially attempted to use patch
104 clamp electrophysiology in the whole-cell configuration to characterize its transport properties.
105 However, unlike for SLC26A9, we did not detect specific currents that could be attributed to
106 SLC26A6 in a wide voltage range. This was irrespective of whether we used symmetric chloride
107 solutions or asymmetric conditions, where the major anion in the extracellular solution was
108 changed to bicarbonate (Figure 1B, Figure 1-Figure Supplement 1B). To confirm the expression
109 of SLC26A6 at the plasma membrane, we employed surface biotinylation and found a similar level
110 as observed for its electrogenic paralog SLC26A9 (Figure 1C). We thus concluded that the
111 transporter would either be inactive, exceedingly slow or that transport would be electroneutral as
112 a consequence of the strict 1:1 exchange of two monovalent anions.

113 Consequently, we turned to *in vitro* assays where we have reconstituted SLC26A6 into
114 proteoliposomes and monitored its activity with ion selective fluorophores. Initially we
115 investigated whether we would be able to detect any sign of uncoupled chloride flow by using a
116 fluorometric assay based on the fluorophore ACMA. This assay monitors pH changes following
117 the ionophore-mediated H^+ influx to compensate for the buildup of a membrane potential during
118 Cl^- uptake, which would enable us to observe transport even if the slow kinetics prevents a
119 characterization by electrophysiology. In this way, we have previously monitored SLC26A9-
120 mediated anion transport into proteoliposomes (Walter et al., 2019). However, in contrast to
121 SLC26A9, no acidification was observed for SLC26A6, emphasizing that the transporter is either
122 inactive or, alternatively, transport would be strictly coupled and electroneutral (Figure 1D).
123 Next, we were interested in whether Cl^- would be exchanged by HCO_3^- by a mechanism where the
124 charges of transported anions are balanced. To this end, we directly monitored Cl^- influx into
125 HCO_3^--loaded proteoliposomes using the fluorophore lucigenin, whose fluorescence is selectively
126 quenched by the former anion. In this assay, we found a robust time-dependent fluorescence
127 decrease at high Cl^- concentration, demonstrating its transport by SLC26A6 (Figure 1E, Figure 1-
128 figure Supplement 1C, D). The process did not require the addition of valinomycin to dissipate the
129 membrane potential, thus underlining that transport is electroneutral. In the investigation of the Cl^-
130 concentration-dependence of transport, we found a saturation with an apparent K_M of about 16-37
131 mM (Figure 1F, Figure 1-figure Supplement 1E). This indicated low affinity for the transported
132 anion is in the same range as observed for Cl^- transport in SLC26A9 (Walter et al., 2019).
133 Finally, we probed whether HCO_3^- itself would be a transported substrate. To this end, we
134 employed a novel HCO_3^--selective europium probe and incorporated this probe within
135 proteoliposomes to assay HCO_3^- influx (Figure 1G) (Martínez-Crespo et al., 2021). The addition

136 of 10 mM HCO_3^- to the outside in presence of a symmetric 200 mM concentration of Cl^- on both
137 sides of the membrane caused a pronounced increase in luminescence that is well above the small
138 non-specific signal observed in liposomes not containing any protein (Figure 1G). This increase is
139 substantially enhanced when using a reduced outside Cl^- concentration of 50 mM to generate an
140 outwardly directed driving force (Figure 1G). Together these experiments demonstrate that HCO_3^-
141 is a transported anion and that its import into proteoliposomes is coupled to the counterflow of Cl^-
142 . Taken together, our experiments underline the function of SLC26A6 as electroneutral coupled
143 Cl^-/HCO_3^- exchanger.
144 Besides HCO_3^-, SLC26A6 was also proposed to be involved in the transport of oxalate in exchange
145 for Cl^- and thus to participate in the excretion of this small divalent anion in both the intestine and
146 kidneys (Clark et al., 2008; Ohana et al., 2013). However, if assuming a coupled 1:1 stoichiometry
147 as observed in case of Cl^-/HCO_3^- exchange, the transported charge would in this case no longer be
148 balanced, thus converting an electroneutral into an electrogenic transport process. As there are no
149 suitable fluorophores for the selective detection of oxalate and since the small dicarboxylic acid
150 also interferes with the detection of Cl^- by lucigenin, we decided to investigate whether a
151 potentially electrogenic Cl^-/oxalate exchange could be assayed with the fluorophore ACMA
152 (Figure 1H, Figure 1-Figure Supplement 1F). In these experiments, we found a robust decrease of
153 the ACMA fluorescence upon the addition of extracellular oxalate to Cl^--loaded proteoliposomes
154 containing SLC26A6, with the concentration dependence and saturation of the fluorescence decay
155 further emphasizing a specific transport process (Figure 1H). We also attempted to follow
156 electrogenic Cl^-/oxalate exchange by patch clamp electrophysiology in the whole cell
157 configuration but did not measure pronounced currents that would be above background, likely
158 due to the slow kinetics of the process (Figure 1-Figure Supplement 1G, H). Together our

159 functional experiments characterize SLC26A6 as a strictly coupled transporter that exchanges Cl^-
160 with HCO_3^- and presumably also oxalate at a 1:1 stoichiometric ratio.
161
162 **SLC26A6 structure**
163 To reveal the molecular basis of the described transport properties of SLC26A6, we have
164 determined its structure by cryo-electron microscopy (cryo-EM). A dataset of the protein purified
165 in the detergent glycol-diosgenin (GDN) at 3.3 Å was of high quality and allowed the unambiguous
166 interpretation of the cryo-EM density by an atomic model (Figure 2A, Figure 2-figure supplements
167 1 and 2). In its organization, the SLC26A6 structure shows familiar features that have previously
168 been observed in various eukaryotic family members of known structure including human and
169 murine SLC26A9 (Chi et al., 2020; Walter et al., 2019), SLC26A5 (Bavi et al., 2021; Butan et al.,
170 2022; Futamata et al., 2022; Ge et al., 2021), SLC26A4 (Liu et al., 2022) and the plant transporter
171 AtSULTR4 (L. Wang et al., 2021) (Figure 2B, Figure 2-Figure Supplement 3). The SLC26A6
172 subunit consists of a membrane-inserted unit (TM) followed by a cytoplasmic STAS domain. In
173 the homodimeric protein, subunit interactions are predominantly formed by the domain-swapped
174 cytoplasmic parts including an extended N-terminal region and the C-terminal STAS domain,
175 whereas the few contacts between the transmembrane transport units are confined to the end of the
176 terminal membrane-spanning helix α14 (Figure 2B). A region connecting secondary structure
177 elements of the STAS domain (located between Cα1 and β4) termed the intervening sequence
178 (IVS) is present in the characterized protein. Previously, removal of this region increased both the
179 stability and surface expression of a construct of the murine SLC26A9 while retaining its transport
180 properties (Walter et al., 2019). In the density, the N-terminal part of the IVS folds into an α-helix
181 encompassing amino acids 569-593 ($C\alpha^{IVS}$) whereas the following 71 residues are unstructured

182 and thus not resolved in the density (Figure 2A). On the C-terminus of the IVS, the density re-
183 appears at Ser 655 at the region preceding β4, which interacts with $C\alpha^{IVS}$ (Figure 2B, C). A
184 generally similar arrangement was also observed in a full-length construct of human SLC26A9
185 (Chi et al., 2020) (Figure 2D). In both structures, $C\alpha^{IVS}$ runs about parallel to the membrane plane
186 and contacts the loop connecting α8 and α9 of the mobile core domain. This presumably influences
187 its conformational preferences thereby potentially impacting transport (Figure 2B-D).
188

189 **The transmembrane domain**

190 In the dimeric transporter, the two TMs share minimal contacts and thus supposedly function as
191 independent units (Figure 2B). Consequently, we expect structural differences underlying the
192 distinct transport properties of SLC26 paralogs to be manifested in this part of the protein. Like in
193 other pro- and eukaryotic family members of known structure, the TMs of SLC26A6 consist of
194 two topologically related repeats of seven transmembrane segments, which span the membrane
195 with opposite orientation (Figure 2-Figure Supplement 3B). Elements of both repeats are
196 intertwined to form two segregated modules, a gate domain and a core domain (Figure 3A). The
197 equivalence between the SLC26A9 and SLC26A6 conformations is illustrated in the overlay of
198 the respective TMs whose Cα positions superimpose with an RMSD of 1.3 Å (Figure 3B). Both
199 conformations represent inward-facing states of transporters presumably functioning by an
200 alternate access mechanism. The substrate binding site located in the center of the core domain is
201 accessible from the cytoplasm via a spacious aqueous cavity, whereas the extracellular exit is
202 sealed by extended contacts between core and gate domains (Figure 3C, D, Figure 3-figure
203 supplement 1A, B). The resemblance between individual sub-domains even exceeds the overall
204 similarity of the TM (with core- and gate domains superimposing with RMSDs of 1.13 Å and 1.2

205 Å, respectively) distinguishing them as largely independent units of a modular protein (Figure 3B).
206 In the comparison of both paralogs, the gate domains do not show pronounced differences (Figure
207 3B). Together with the cytoplasmic STAS domains, which constitute the bulk of the dimer
208 interface, these sub-domains form a contiguous rigid scaffold of the dimeric protein that
209 presumably remains static during transport (Figure 2B, Figure 3-figure supplement 1C). In
210 contrast, both core domains represent the mobile elements of the protein (Figure 3-figure
211 supplement 1D). Each core domain carries a substrate binding site located in a pocket at the center
212 of the unit facing the gate domain (Figures 3C, D and 4A). The presumable location of a bound
213 chloride ion is resolved in the structure of SLC26A6 at a low contour of the map (Figure 4B, Figure
214 2-figure supplement 2B). This position concurs with positions inferred from known structures of
215 paralogs, which show binding of Cl^- and HCO_3^- to an equivalent location (Chi et al., 2020;
216 Futamata et al., 2022; Ge et al., 2021; Liu et al., 2022) (Figure 4B, Figure 4-figure supplement 1).
217 The anion binding site is placed between the opposed short helices α3 and α10, which partly span
218 the membrane and whose N-termini are aligned to face each other in the center of the core domain
219 (Figure 4A). Together with the sidechains of surrounding residues, both α-helix termini form a
220 selective anion binding site (Figure 4B-G, Figure 4-figure supplement 1). In complex with its
221 bound cargo, the core domain is believed to shuttle as rigid unit between two extreme
222 conformations where the binding sites are either exposed to the cytoplasm or the extracellular
223 environment (Figure 3C, D, Figure 3-figure supplement 1D).
224 As carrier of the substrate binding site, the core domains presumably display the characteristic
225 features accounting for the distinct functional properties of SLC26A6 and SLC26A9. Their
226 conservation within the SLC26 family is illustrated in the comparison of the respective domains
227 of SLC26A6 and SLC26A5 (Prestin) (Figure 4C, Figure 4-figure supplement 1A, C, D, E, G).

228 Latter belongs to a protein that, instead of transporting ions, confers electromotility and which in
229 the best defined structure (PDBID 7LGU) resides in a distinct conformation where the substrate
230 binding site has become buried between core and gate domain (leading to an RMSD of 2.9 Å for
231 the entire TMD) (Ge et al., 2021). Despite the functional and conformational differences, the core
232 domains of both proteins superimpose with an RMSD of only 1.13 Å, illustrating their close
233 structural resemblance (Figure 4-figure supplement 1A, C). Although not working as transporter,
234 both proteins share similar ion binding properties that extends to Cl^- and HCO_3^-, latter of which is
235 not a substrate of SLC26A9 (Walter et al., 2019). In contrast to the general similarity with
236 SLC26A5, the comparison of the same units of SLC26A6 and SLC26A9 shows distinct features
237 that likely underlie the differences in substrate selectivity and transport mechanism (Figure 4-
238 figure supplement 1B, C). These are confined to the conformation of α10, which at its N-terminus
239 forms direct interactions with transported ions, whereas the remainder of the domain is very similar
240 (Figure 4-figure supplement 1B, C). The difference in the conformations of this short membrane-
241 inserted helix can be approximated by a 12-14º rotation of α10 of SLC26A9 around an axis located
242 at its C-terminal end towards α-helix 1 (Figure 4F, Figure 4-figure supplement 1B, C). The
243 replacement of residues within the contact region of SLC26A9 in comparison to other family
244 members acts to lower their side chain volume at the contact region between both helices (Figure
245 4C-F). These include Ser 96 and Val 100 on SLC26A6, which are both replaced by glycines at
246 equivalent positions in SLC26A9 (i.e., Gly 77 and Gly 81) and a substitution of Val 407, Gln 408
247 and Thr 411 by Ala 396, Val 397 and Ala 400 (Figure 4C-F). In addition to the described
248 substitutions, there are also differences in the side-chains surrounding the ion binding site, which
249 together determine the size and polarity of the substrate binding pocket (Figure 4C, G-I). These
250 differences extend to Ser 401 of SLC26A6, which is replaced by an alanine in SLC26A9 (Ala

251 390), and most prominent, the large Arg 404 of SLC26A6, which is replaced by Val 393 in
252 SLC26A9 (Figure 4C, D-I, Figure 4-figure supplement 1D-G). As a result, the pocket is
253 considerably deeper in SLC26A9 compared SLC26A6, where it is delimited by the side chain of
254 Arg 404 that interacts with the residues preceding α helix 3 to form the back side of the shallow
255 binding site (Figure 4D-I, Figure 4-figure supplement 1D-H). In addition to its structural role, Arg
256 404 likely also contributes to the stabilization of bound anions by coulombic interactions, with its
257 guanidium group potentially engaging in direct interactions with bicarbonate or oxalate. The
258 altered geometry of the site leads to the binding of Cl^- deeper in the pocket in case of SLC26A9
259 (Figure 4G-I, Figure 4-figure supplement 1H) and presumably explains why bicarbonate interacts
260 with SLC26A6 but not SLC26A9.
261
262 **Structure-function relationships**
263 Whereas our functional data has defined SLC26A6 as a coupled antiporter that exchanges Cl^- with
264 either HCO_3^- or oxalate at equimolar stoichiometry, its structure has revealed the architecture of a
265 transport protein in an inward-facing conformation where the transport properties are presumably
266 determined by the detailed organization of the mobile core domain. This protein module shows
267 pronounced structural differences compared to the equivalent unit of the uncoupled transporter
268 SLC26A9, resulting in a remodeled anion binding site, which in SLC26A6 is lined by a conserved
269 basic residue (i.e., Arg 404) that is ubiquitous in other mammalian paralogs (Figure 4C and 5A).
270 We thus decided to mutate this position to the amino acid found in SLC26A9 and to characterize
271 the transport properties of the SLC26A6 mutant R404V. This mutation is well-tolerated and does
272 not interfere with protein integrity as judged by its expression level and biochemical properties.
273 We initially investigated whether SLC26A6 R404V would conduct ions as a consequence of

274 compromised coupling properties and thus studied the protein by patch-clamp electrophysiology.
275 In whole-cell patch clamp experiments, we detected small currents in symmetric Cl^- solutions,
276 which are low compared to SLC26A9, despite the comparable expression of the mutant at the cell-
277 surface (Figure 5B-D). Irrespective of their magnitude, these currents are indicative for the
278 capability of the protein to mediate electrogenic Cl^- transport. We thus turned to our
279 proteoliposome-based ACMA assay to confirm that sidechain replacement has indeed conferred
280 the ability to SLC26A6 to pass downhill Cl^- transport (Figure 5E). After demonstrating uncoupled
281 chloride transport, we tested whether the mutant has retained its ability of mediating coupled Cl^-
282 $/HCO_3^-$ exchange using the fluorophore lucigenin but did not find pronounced Cl^- flux in this case
283 (Figure 5F, G). Together our data suggest that the mutation of a conserved basic position in the
284 ion binding site has compromised the ability of SLC26A6 to mediate coupled Cl^-/HCO_3^- exchange
285 and instead facilitated uncoupled Cl^- transport with slow kinetics. While these findings underline
286 the importance of Arg 404 for anion interactions and coupling, they also emphasize that the
287 mutation of a single residue is insufficient to confer the complete functional phenotype of
288 SLC26A9 as a fast uncoupled Cl^- conductor. Nevertheless, our results further underline the
289 importance of the anion binding site in SLC26 transporters for the transport mechanism of its
290 members.
291

292 **Discussion**

293 By combining structural data obtained by cryo-EM with electrophysiology and transport assays,
294 our study has elucidated the previously unknown architecture of SLC26A6, defined its transport
295 properties and revealed the features that underlie the mechanistic distinction to the paralog
296 SLC26A9. By using a novel HCO_3^- selective europium probe (Martínez-Crespo et al., 2021), we

297 have directly demonstrated the transport of this important physiological anion (Figure 1G). We
298 have further clarified the controversy concerning the transport mechanism of SLC26A6 (Ohana et
299 al., 2009) by detecting a strict equimolar exchange of anions binding to a conserved site in the
300 mobile core domain of the transmembrane transport unit (Figure 4B, H). Consequently, this
301 exchange is electroneutral in case of the monovalent HCO_3^- and electrogenic in case of the divalent
302 oxalate (Figure 1E-H).
303 Regarding their function, SLC26A6 and SLC26A9 show distinct features with respect to substrate
304 selectivity and the general transport mechanism (Ohana et al., 2009). Remarkably, both proteins
305 are capable of interacting with Cl^- with similar mM affinity (Figure 1F) (Walter et al., 2019).
306 However, they do this via distinct interactions in equivalent binding regions. In SLC26A9, Cl^-
307 binds in a deep pocket with low field strength, whereas the same pocket is shallower in SLC26A6,
308 where a conserved arginine (Arg 404) increases the positive electrostatic potential and thus likely
309 stabilizes the bound anion (Figures 4H, I and 6). Together with the presence of additional residues
310 at the binding site (i.e., Ser 401 at the N-terminal end of α11), the captured Cl^- in SLC26A6 thus
311 can rely on a larger density of polar interactions (Figure 4-extended data fig. 1E, F). The same site
312 likely also provides a suitable environment for HCO_3^- and oxalate, neither of which are substrates
313 of SLC26A9 (Dorwart et al., 2007; Walter et al., 2019). A similar anion interaction observed in
314 SLC26A6 is also found in the paralogs SLC26A4 (Pendrin) (Liu et al., 2022) and SLC26A5
315 (Prestin) (Futamata et al., 2022; Ge et al., 2021), which both share a comparable substrate
316 preference. The similarity between the core domains of SLC26A6 and Prestin is remarkable in
317 light of the altered function of the latter, which is no longer capable of transport and instead
318 operates as motor protein in cochlear outer hair cells of mammals (Zheng et al., 2000). While to
319 some degree Prestin undergoes comparable conformational changes as other family members, as

320 illustrated in the similarity of the structures of intermediate conformations of SLC26A9 and
321 SLC26A5, the full transition into an outward-facing conformation to release the bound anion to
322 the extracellular environment appears in this case to be prohibited (Bavi et al., 2021; Ge et al.,
323 2021).
324 Besides the absence of a residue carrying a positive charge, the altered binding site in SLC26A9
325 is also a consequence of concerted replacements of interacting amino acids on α1 and α10, which
326 change the immediate environment of the bound ion and allow for a reorientation of the partly
327 inserted helix α10 whose N-terminus contributes part of the interactions (Figure 4C, D).
328 Collectively, these changes presumably lead to the altered ion selectivity. The importance of the
329 described anion binding site for the transport mechanism is illustrated in the point mutation R404V
330 in SLC26A6. The replacement of this basic residue, which was considered a hallmark in the
331 distinction between SLC26A9 and other family members (Walter et al., 2019) has compromised
332 coupled Cl^-/ HCO_3^- exchange and instead mediates uncoupled Cl^- transport, although with slower
333 kinetics than SLC26A9 (Figures 5B-G, 6).
334 From a mechanistic viewpoint SLC26A9 and SLC26A6 are distinguished by the sequence of
335 conformations that together define the transport cycle (Figure 6). In the uncoupled SLC26A9, the
336 transporter is able to transition between inward- and outward facing states at a high rate, which
337 underlies the pronounced currents observed in patch clamp experiments (Figure 6B, Figure 1-
338 figure supplement 1A). The same change of the access in an unloaded conformation is kinetically
339 unfavorable in the coupled exchanger SLC26A6, as illustrated in the lack of current in
340 electrophysiological recordings and the absence of a Cl^- leak in a vesicle-based assay (Figures 1B-
341 D and 6A, Figure 1-figure supplement 1B). The basis for the distinctive kinetic features of both
342 paralogs is currently still unclear, and we do at this stage not exclude the existence of a leaky

343 channel-like conformation in SLC26A9. Such a conformation could potentially promote Cl^- flow
344 across a continuous aqueous pore without obligatory protein movement, although there is currently
345 no structural evidence for its existence. The nature of the energy barrier, which prevents the
346 shuttling of the unloaded state of SLC26A6 and other paralogs with similar functional phenotype
347 (*i.e.*, the transporters SLC26A1-4) has thus far remained elusive. It is likely that conformational
348 changes are dictated by interactions between the mobile core domain with the immobile gate
349 domain, which are both believed to operate as semi-independent entities (Geertsma et al., 2015;
350 Walter et al., 2019). Remarkably, both units bury a similar contact area in the inward-facing
351 conformations of SLC26A6 and SLC26A9 and do not exhibit pronounced differences in their
352 interactions (Figure 3-figure supplement 1A, B). Additional contacts in SLC26A6 are established
353 with the structured N-terminal part of the IVS region of the STAS domain of the interacting
354 subunit, which appear to further stabilize the observed inward-facing conformation (Figure 2C).
355 Similar interactions have also been found in the full-length transporter SLC26A9 (Chi et al., 2020),
356 which, next to the increased surface expression, could account for the strongly increased activity
357 observed in the construct $SLC26A9^T$ where the IVS sequence of the protein was removed (Walter
358 et al., 2019). Besides the effect of the IVS, also the truncation of the C-terminus of SLC26A9
359 might have contributed to this high activity. These unstructured C-termini are weakly conserved
360 and contain a PDZ binding motif at its end, which is believed to tether either transporter to potential
361 partners such as the anion channel CFTR or the Na^+ dependent citrate carrier SLC13A2 via
362 interacting scaffolding proteins (Ohana et al., 2013; Shcheynikov, Ko, et al., 2006). In the isoform
363 b of SLC26A9, a C-terminal extension was located in the aqueous cavity leading to the substrate
364 binding site in the inward-facing conformation of SLC26A9, thereby locking the transporter in the
365 observed conformation (Chi et al., 2020) (Figure 2-Figure Supplement 3A). There is no similar

366 extension found in any SLC26A6 isoforms, and the role of this interaction in a cellular
367 environment is currently unclear, although it hints at a possible regulation in SLC26A9.
368 Collectively our study has provided key insight into the structural basis for substrate selectivity
369 and the mechanistic distinction between uncoupled and coupled transporters of the SLC26 family
370 and thus provides a foundation for future investigations.
371

372 **Material and Methods**

373 **Key resources table**

Reagent type	**Designation**	**Source or reference**	**Identifiers**	**Additional information**
Chemical compound, drug	HyClone HyCell TransFx-H medium	Cytiva	SH30939.02	
Chemical compound, drug	1-palmitoyl-2-oleoyl-sn-glycero-3-phosphoethanolamine (16:0-18:1 PE POPG)	Avanti Polar Lipids	850757C	
Chemical compound, drug	1-palmitoyl-2-oleoyl-glycero-3-phosphocholine (16:0-18:1 PC (POPC)	Avanti Polar Lipids	850457C	
Chemical compound, drug	Cholesterol	Sigma	C8667	
Chemical compound, drug	Triton X-100	Sigma	T9284	

Chemical compound, drug	Pepstatin A	Axon lab	A2205.0100	
Chemical compound, drug	Phenylmethylsulfonyl fluoride (PMSF)	Sigma	PMSF-RO	
Chemical compound, drug	Leupeptin	AppliChem	A2183,0100	
Chemical compound, drug	Benzamidine	Sigma	B6506	
Chemical compound, drug	Chloroform	Fluka	25690	
Chemical compound, drug	GDN	Anatrace	GDN101	
Chemical compound, drug	Diethyl ether	Sigma	296082	
Chemical compound, drug	DNase I	AppliChem	A3778	
Chemical compound, drug	Glycerin, Glycerol 86%	Roth	4043.3	
Chemical compound, drug	HCl	Merck Millipore	1.00319.1000	
Chemical compound, drug	HEPES	Sigma	H3375	
Chemical compound, drug	$[Eu.L1]^+$	Loughborough University (Dr SJ Butler)	N/A	
Chemical compound, drug	ACMA	Thermofischer Scientific	A1324	

Chemical compound, drug	CCCP	Sigma	C2759	
Chemical compound, drug	*N,N′*-Dimethyl-9,9′-biacridinium-dinitrat (Lucigenin)	Sigma	M8010	
Chemical compound, drug	Phosphate buffered saline	Sigma	D8537	
Chemical compound, drug	Strep-Tactin® Superflow® high capacity resin	IBA	2-1208-010	
Chemical compound, drug	D-desthiobiotin	Sigma	D1411	
Chemical compound, drug	Kolliphor P188	Sigma	K4894	
Chemical compound, drug	L-glutamine	Sigma	G7513	
Chemical compound, drug	Penicillin-streptomycin	Sigma	P0781	
Chemical compound, drug	Fetal bovine serum	Sigma	F7524	
Chemical compound, drug	Polyethylenimine 25 K MW, linear	Polysciences	23966–1	
Chemical compound, drug	40kDa linear PEI MAX	Polysciences	24765-1	
Chemical compound, drug	Valproic acid	Sigma	P4543	
Chemical compound, drug	Calcium Chloride	Sigma	223506	

Chemical compound, drug	Magnesium Chloride	Fluka	63,065	
Chemical compound, drug	Potassium chloride	Sigma	746346	
Chemical compound, drug	Sodium chloride	Sigma	71380	
Chemical compound, drug	Terrific broth	Sigma	T9179	
Chemical compound, drug	Mouse-anti-myc primary antibody	Sigma	M4439	
Chemical compound, drug	Peroxidase AffiniPure Goat Anti-Mouse IgG (H+L)	Jackson ImmunoResearch	115-035-003	RRID: AB 10015289
Commercial assay or kit	4–20% Mini-PROTEAN® TGX™ Precast Protein Gels, 15-well, 15 µl	BioRad Laboratories	4561096DC	
Commercial assay or kit	Amicon Ultra-4 Centrifugal Filters Ultracel 100K, 4 ml	Merck Millipore	UFC810024	
Commercial assay or kit	Borosilicate glass capillary with filament Sutter	Instrument	BF150-86-10HP	
Commercial assay or kit	0.22 µm Ultrafree-MC Centrifugal Filtfer	EMD Millipore	UFC30GV	
Commercial assay or kit	Biobeads SM-2 adsorbents	BioRad Laboratories	152-3920	
Commercial assay or kit	Avestin Extruder kit	Sigma	Z373400	

Commercial assay or kit	Pierce™ Cell Surface Biotinylation and Isolation Kit	Thermofischer Scientific	A44390	
Commercial assay or kit	Amersham ECL Prime Western Blotting Detection Reagent	Cytiva	RPN2232	
Commercial assay or kit	Polycarbonate Membranes 400nm	Sigma	610007	
Commercial assay or kit	Polycarbonate Membranes 50nm	Sigma	610003	
Commercial assay or kit	96-well black walled microplates	Thermofischer Scientific	M33089	
Commercial assay or kit	384-well black microplate flat-bottom	Grenier	781076	
Commercial assay or kit	Quantifoil R1.2/1.3 Au 200 Mesh	Electron Microscopy Sciences	Q2100AR1.3	
Commercial assay or kit	Superose 6 10/300 GL	Cytiva	17517501	
Other	BioQuantum Energy Filter	Gatan	N/A	
Other	HPL6	Maximator	N/A	
Other	K3 Direct Detector	Gatan	N/A	
Other	Titan Krios G3i	ThermoFisher Scientific	N/A	

Other	Viber Fusion FX7 imaging system	Witec	N/A	
Other	TECAN M1000 Infinite	TECAN	N/A	
Other	TECAN SPARK	TECAN	N/A	
Other	Vitrobot Mark IV	ThermoFisher Scientific	N/A	
Cell line	HEK293 GnTi- & HEK293T	ATCC	CRL-3022 & CRL-1573	
recombinant DNA	Mammalian expression vector with C-terminal 3C cleavage site, venus tag, myc tag, SBP tag.	Dutzler laboratory	N/A	
recombinant DNA	Mus musculus SLC26A9 ORF shuttle clone	BioScience	GenBank BC160193	
recombinant DNA	Homo sapiens SLC26A6 cDNA clone	BioScience	GenBank BC017697	
recombinant protein	HRV 3C protease	Expressed (pET_3C) and purified in Dutzler laboratory	N/A	
Software, algorithm	ASTRA7.2	Wyatt Technology	https://www.wyatt.com/products/software/astra.html	RRID: SCR_016255
Software, algorithm	ChimeraX 1.4	Pettersen et al., 2021	https://www.rbvi.ucsf.edu/chimerax/	RRID: SCR_015872
Softwate, algorithm	Biorender		https://app.biorender.com/biorender-templates	

Software, algorithm	Coot v.0.9.4	Emsley et al., 2010	https://www2.mrc-lmb.cam.ac.uk/personal/pemsley/coot/	RRID: SCR_014222
Software, algorithm	cryoSPARC v3.2.0-4.0	Structura Biotechnology Inc.	https://cryosparc.com/	RRID: SCR_016501
Software, algorithm	DINO		http://www.dino3d.org	RRID: SCR_013497
Software, algorithm	EPU2.9	ThermoFisher Scientific	N/A	
Software, algorithm	Phenix	Liebschner et al., 2019	https://www.phenix-online.org/	RRID: SCR_014224
Software, algorithm	DeepEMhancer	Sanchez-Garcia et al., 2021	https://github.com/rsanchezgarc/deepEMhancer	
Software, algorithm	JALVIEW	Waterhouse et al., 2009		
Software, algorithm	Muscle	Edgar, 2004		
Software, algorithm	Axon Clampex 10.6	Molecular Devices	N/A	
Software, algorithm	Axon Clampfit 10.6	Molecular Devices	N/A	
Software, algorithm	Prism 9	GraphPad	N/A	
Strain	E. coli MC1061	ThermoFisher Scientific	C66303	

374

375 **Construct Generation**

376 The open reading frame of human SLC26A6 (isoform 3) (GenBank accession number: BC017697)
377 and mouse SLC26A9 (GenBank accession number: BC160193) was amplified from a cDNA clone
378 (Source BioScience) and cloned into into a pcDNA 3.1 vector (Invitrogen) modified to be
379 compatible with the FX-cloning (Geertsma & Dutzler, 2011). The truncated murine SLC26A9
380 construct (SLC26A9T) was generated as previously detailed (Walter et al., 2019). All FX-modified
381 expression constructs contained a C-terminal C3 protease cleavage site, venus YFP, myc-tag and
382 streptavidin-binding protein (SBP). To introduce the R404V mutation to hSLC26A6, the
383 QuickChange (Aligent) mutagenesis method was used with the following primers: Forward: 5'-
384 GCT CTA TGT CTG TGA GCC TGG TAC-3' and Reverse: 5'-GTA CCA GGC TCA CAG ACA
385 TAG AGC-3'.

386

387 **Protein Expression**

388 Suspension HEK HEK293S GnTI^{-} cells (ATCC CRL-3022) were grown and maintained in
389 HyClone TransFx-H (GE Healthcare) media supplemented with 1% FBS, 1% Kolliphor P188, 100
390 U ml^{-1} penicillin/streptomycin & 2mM Glutamine. Cells were incubated at 37 ºC & 5% CO_2 in
391 TubeSpin Bioreactor 600 vessels (TPP) and shaken at 185 rpm.

392 For transient transfections, cells were split for transfection 24 h prior from a cell density of 1-1.5
393 10^6 ml^{-1} to 0.4-0.6 10^6 ml^{-1}. A ratio of 1.2µg Plasmid DNA per 10^6 cells and 40kDa linear PEI
394 MAX (Polysciences) transfection reagent were utilised for protein expression. On the day of
395 transfection, a 10µg.ml^{-1} DNA dilution was incubated in non-supplemented DMEM media
396 (Sigma). Linear PEI MAX was incubated with DNA to a ratio of 1:3 (w/w) from a 1 mg ml^{-1} stock.

397 After a 15-minute incubation, the DNA-PEI mix was added to suspension cells and co-incubated
398 3mM valproic acid (VPA). Cells were harvested after 48 h expression and flash-frozen in liquid
399 N_2 prior to storage at -80 ºC.

400

401 **Protein Purification**

402 For protein purification, all protocols were performed at 4ºC. Cell pellets were thawed and mixed
403 with extraction buffer (25 mM HEPES, pH 7.4, 200 mM NaCl, 5% glycerol, 2 mM $CaCl_2$, 2 mM
404 $MgCl_2$, 2% GDN, benzamidine 1 mM, leupeptin 10 µM, pepstatin A 1 µM, PMSF 100 µM). Cell
405 lysis was incubated for 2 h at 4 ºC prior to ultracentrifugation (85,0000 g, 30 min, 4 ºC) to remove
406 insoluble material. Lysate was filtered (5µm filter, Sartorius) prior to binding to Streptactin
407 Superflow high-capacity resin (IBA Lifesciences) equilibrated in wash buffer (25 mM HEPES, pH
408 7.4, 200 mM NaCl, 5% glycerol, 0.02% GDN) for 2 h.

409 After discarding the flow-through of clarified lysate through gravity flow, Streptactin resin was
410 washed with 40 column volumes (CV) wash buffer and SBP-tagged protein was eluted using wash
411 buffer supplemented with 10 mM desthiobiotin (Sigma). Eluate was concentrated to 500 µl using
412 a 100 KDa MWCO concentrator (amicon), pre-equilibrated in wash buffer. C-terminal purification
413 and detection tags were cleaved by 3C protease at a 2:1 protease:protein mass ratio. Prior to size-
414 exclusion chromatography, samples were passed through a 0.22 µm filter (Millipore). Samples
415 were injected on the Äkta prime plus chromatography system (Cytivia) and separated on a
416 Superose 6 10/300 column (GE Healthcare) in SEC buffer (10 mM HEPES, pH 7.4, 200 mM NaCl,
417 0.02% GDN). Protein containing peak samples were collected and used for cryo-EM sample
418 preparation at a 2 mg ml^{-1} concentration or used immediately for liposome reconstitution.

419

420 **Surface biotinylation**

421 Adherent HEK293T cells were transfected at 80% confluency were transfected with 10 µg of
422 plasmid encoding SLC26A6 WT and R404V constructs fused with a c-terminal SBP-Myc-Venus
423 tag per 10 cm culture dish. Transfection was performed using PEI MAX at a DNA:PEI ratio of
424 1:4. The Pierce™ Cell Surface Biotinylation and Isolation Kit (Themo Fisher) was used according
425 to manufacturer's guidelines. Cells were washed with PBS from 10 ml culture per construct and
426 biotinylated following 24 h of expression using EZ-Link Sulfo-NHS-SS-Biotin. Quenching was
427 then performed using 750 µl quenching buffer and cells were harvested. Following a PBS wash-
428 step and centrifugation at 1000 g, cells were re-suspended and lysed in 200 µl extraction buffer
429 (25 mM HEPES, pH 7.4, 200 mM NaCl, 5% glycerol, 2 mM $CaCl_2$, 2 mM $MgCl_2$, 2% GDN,
430 benzamidine 1 mM, leupeptin 10 µM, pepstatin A 1 µM, PMSF 100 µM) by gentle agitation for
431 1 h at 4 °C. Insoluble fractions were removed by centrifugation at 50,000 *g* for 30 min and
432 supernatant was incubated with 200 µl Neutravidin agarose slurry pre-equilibrated in wash buffer
433 (25 mM HEPES, pH 7.4, 200 mM NaCl, 5% glycerol, 0.02% GDN) for 1 h at 4ºC. The resin was
434 washed 3 times with 200 µl of wash buffer and surface-biotinylated proteins were eluted by
435 incubation with 200 µl wash buffer containing 50 mM fresh DTT for 1 h at 4 ºC with gentle mixing
436 of the sample. 20 µl of input, flow-through and surface-eluted samples were separated by SDS-
437 PAGE. Samples were then transferred to a PVDF membrane and analyzed by Western blot using
438 a mouse-anti-myc primary antibody (Sigma) and HRP-coupled goat-anti-mouse secondary
439 antibody (Jackson ImmunoResearch). Antibodies were diluted 1:10,000 in TBS-T with 5%
440 skimmed milk. Chemoluminescence signal was developed using ECL prime reagent (Cytiva) and
441 imaged using a Fusion FX7 imaging system (Vilber).

442

443 **Liposome Reconstitution**

444 For liposome reconstitutions using the [Eu.L1$^+$] bicarbonate-selective probe, lipid preparation was
445 performed on the same day as protein purification. POPE:Cholesterol lipids (7:3 w/w ratio, Avanti)
446 were pooled in a round-bottom flask and initially dried under N_2 flow to form a lipid film. Lipids
447 were further dried under vacuum for 1 h prior to re-hydration with [Eu.L1$^+$] buffer (50 μM
448 [Eu.L1$^+$], 200 mM NaCl, 5 mM HEPES, pH 7.4). The resulting suspension was gently sonicated
449 and stirred for 2 h to generate a homogeneous mixture. Ten freeze-thaw cycles were performed to
450 generate multilamellar liposomes before extrusion 29 times through x2 polycarbonate 400 nm
451 filters to give unilamellar liposomes.

452 For protein incorporation, incremental 10 μl additions of 10% Triton X-100 (w/v) were performed
453 and monitoring of absorbance at 540 nm was used to detect liposome destabilization. After the
454 formation of stabilized liposomes, purified SLC26A6 was added at an lipid-to-protein ratio (LPR)
455 of 50:1. To counteract [Eu.L1$^+$] probe leakage, an additional equimolar 50 μM [Eu.L1$^+$] was
456 added. The subsequent mixture was gently rotated at RT for 20 min prior to an addition of 250 mg
457 SM-2 Bio-Beads (Bio-Rad) per 5 ml of sample. The sample was then incubated for 30 min at RT
458 prior to incubation at 4 ºC. Bio-Bead additions were performed over a three-day period every 24
459 h. Biobeads were removed by gravity filtration and the sample was used immediately for assay
460 measurements.

461 For liposome reconstitutions for the Lucigenin and ACMA assays, a similar procedure was used
462 with the following adjustments. POPE:POPG lipids (3:1 w/w) were first pooled in a round-bottom
463 flask and washed with diethyl ether prior to drying under N_2 for 1.5 h. Lipids were then dissolved

464 to 20 mg/ml in 10 mM HEPES, 150 mM KCl prior to sonication to form a homogeneous mixture.
465 After three freeze-thaw cycles the sample was frozen in liquid N_2 and stored at -80 ºC until further
466 use. Purified SLC6A9T was incorporated utilizing the triton-destabilisation method previously
467 detailed at a LPR of 80:1 (w/w). Both SLC26A6 wildtype and the R404V mutant were
468 incorporated at a 50:1 (w/w) ratio. Subsequently, successful incorporation was confirmed by SDS-
469 PAGE gel quantification. For all reconstitution procedures, mock empty liposomes lacking any
470 purified protein were generated using the same protocols.

471

472 **[Eu.L1$^+$] Bicarbonate Transport Assay**

473 For all measurements of HCO_3^- transport, buffers used were degassed to remove atmospheric CO_2.
474 After Bio-Bead removal via gravity filtration, proteoliposomes were pelleted and the excess
475 [Eu.L1$^+$] probe (Martínez-Crespo et al., 2021) washed by sequential ultracentrifugation and
476 resuspension steps in outside buffer (200 mM NaCl, 5 mM HEPES, pH 7.4). Where 50 mM
477 internal NaCl was required, liposomes were pelleted by ultracentrifugation and resuspended in
478 asymmetric internal buffer (50 µM [Eu.L1$^+$], 50 mM NaCl, 5 mM HEPES, pH7.4). Liposomes
479 were further subjected to five freeze-thaw cycles and extruded 29 times using 400 nm
480 polycarbonate filters. Sequential ultracentrifugation wash steps were performed before
481 resuspension in outside buffer.

482 For measurements of electroneutral Cl^-/ HCO_3^- exchange, 100 µl of SLC26A6 proteoliposomes
483 were added to a 96-well flat bottom black plate (Grenier). Prior to measurement, liposome samples
484 were gently bubbled under N_2 for 2 min to remove atmospheric CO_2 and residual HCO_3^- from
485 samples. Following the recording of a baseline emission for 20 cycles (lasting 0.5 s each), 10 mM

486 HCO_3^- was added and normalized [Eu.L1+] emission (excitation = 332, emission= 617) was
487 determined following lysis of liposomes by 0.4 % Triton after cycle 300. Time gating of the
488 recorded emission was performed using a 150µs lag-time between excitation and signal integration
489 with an overall 850µs integration time. HCO_3^- transport by was measured in the presence of both
490 four-fold NaCl gradient (200 mM inside/50 mM outside) and symmetrical conditions (200 mM
491 inside/200 mM outside).

492

493 **ACMA Assay**

494 To compare uncoupled chloride properties of SLC26A6 to SLC26A9, proteoliposomes were
495 prepared to obtain an internal buffer concentration of 50 mM Na_2SO_4, 10 mM HEPES, pH 7.
496 Proteoiposomes were sonicated in 20 µl aliquots to form unilamellar vesicles prior to dilution into
497 9-amino-6-chloro-2-methoxyacridine (ACMA) assay buffer (2 µM ACMA, 75 mM NaCl, 10 mM
498 HEPES, pH 7.4). 100 µl aliquots were added to a 96-well plate and after a baseline measurement
499 period for 13 cycles (0.5 s per cycle), the protonophore carbonyl cyanide 3-chlorophenylhydrazone
500 (CCCP) was added to dissipate the membrane potential and permit transporter-mediated anion-
501 movement. ACMA fluorescence (excitation = 412 nm and emission = 482 nm), as a determinant
502 of Cl^- transport, was measured using the Tecan Infinite M1000 Pro Plate Reader over 495 seconds
503 or using the Tecan Spark Plate reader over 1,800 s. Data are normalized to the point of CCCP
504 addition.

505 To measure electrogenic oxalate transport, the same protocol was applied with the following
506 exception: SLC26A6 liposomes consisted of an internal concentration of 150 mM KCl, 10 mM

507 HEPES, pH 7.4. 40 µl aliquots were added to a to a black 384-well plate (Grenier) and ACMA
508 fluorescence was measured on a TECAN Spark Plate Reader over 1,200 s.

509

510 **Lucigenin Assay**

511 For measurement of anion transport mediated by Cl^-/ HCO_3^- exchange, the halide-sensitive
512 lucigenin dye (400 µM) was incorporated into proteoliposomes containing either SLC26A6 or
513 SLC26A6 R404V mutant and empty mock liposomes (all with a POPE:POPG composition of 3:1
514 w/w) in 200 mM HCO_3^-, 10 mM HEPES, pH 7.4. To permit fluorophore incorporation, liposomes
515 were diluted in the above buffer and three freeze-thaw cycles were performed prior to extrusion
516 (17 times) using 50 nm polycarbonate filters. Sequential ultracentrifugation and resuspension in
517 assay buffer containing no lucigenin dye were performed to remove excess exterior lucigenin. 40
518 µl aliquots were transferred to a black 384-well plate and after 20 cycles (0.2 second per cycle), 0
519 to 240 mM NaCl diluted in assay buffer was added. Quenching of lucigenin fluorescence
520 (excitation = 430 nm, emission = 505 nm) was measured as a determinant of chloride influx for
521 300 cycles prior to lysis by 0.4% Triton. Data are normalized to the point of NaCl addition and
522 corrected for signal observed under mock liposome conditions.

523

524 **Electrophysiology**

525 For electrophysiology recordings, adherent HEK293T cells (ATCC) were maintained in DMEM
526 (Gibco) media and incubated at 37 ºC and 5% CO_2. Media was supplemented with 10% FBS, 1
527 mM L-glutamine, 4.5 g l^{-1} Glucose, 1 mM sodium pyruvate and 100 U ml^{-1} penicillin/streptomycin
528 (Sigma). Cells were transfected at between 40-60% confluency and split into 60 x 15 mm dishes

529 (Corning) the day prior to transfection. Plasmid DNA was transfected at a concentration of 5 µg
530 DNA together with linear PEI (25 kDa) at a ratio of 1:2.5 (w/w) DNA to PEI. DNA and PEI were
531 mixed in non-supplemented media, incubated at RT for 10 min and added dropwise to cells with
532 3 mM VPA. Venus-fused constructs of human SLC26A6 and mouse SLC26A9 were used for
533 recordings to allow for detection of expression through fluorescence microscopy. Cells were
534 recorded from between 16-30 h post-transfection.

535 Patch pipettes were formed from pulled and polished borosilicate glass capillaries (OD = 1.5 mm,
536 ID = 0.86 mm, Sutter). When backfilled with 150 mM CsCl, patch pipettes yielded a resistance of
537 between 2-4 MΩ. For voltage-clamp experiments, currents were recorded with an Axopatch 200B
538 amplifier and digitized using a Digidata 1440A A/D converter. Signals were filtered at 5 kHz and
539 sampled at 20 kHz prior to acquisition with Clampex 10.6 (Molecular Devices). Recorded cell
540 capacitance upon break-in varied between 10-30 pF with series resistance <10 MΩ and calculated
541 liquid junction potentials (JPCalcW, Molecular Devices) never surpassed 5 mV.

542 For whole-cell patch-clamp experiments, the intracellular pipette solution consisted of 146 mM
543 CsCl, 2 mM MgCl2, 5 mM EGTA, 10 mM HEPES and pH 7.4. Extracellular bath solutions
544 consisted of either 146 mM CsCl, 2 mM MgCl2, 5 mM EGTA, 10 mM HEPES or 150 mM
545 $CsHCO_3$/150 mM Cs_2Oxalate, 2mM $Mg(OAc)_2$, 5 mM EGTA, 10 mM HEPES with pH adjusted
546 using either CsOH or methanesulfonate. The pH of HCO_3^- was monitored to ensure the production
547 of CO_2 and decline of HCO_3^- never exceeded 20%. All acquired electrophysiology data were
548 analyzed using Clampfit 11.0.3 (Molecular Devices), Excel (Microsoft), and GraphPad Prism 9
549 (GraphPad).

550

551 **Cryo-EM Data Acquisition**

552 To proceed with cryo-EM structural determination, 2.5 µl samples of GDN-purified SLC26A6
553 was applied to glow-discharged holey carbon grids (Quantifoil R1.2/1.3 Au 200 mesh) at a
554 concentration of 2 mg ml^{-1}. Blotting of the sample (3-6 s) was performed at 4 ºC at a relative
555 humidity of 75% and grids were flash-frozen in liquid propane-ethane mix with a Vitrobot Mark
556 IV (Thermo Fisher Scientific). A total of 11,962 images from two combined datasets were
557 collected on a 300 kV Titan Krios G3i using a 100 µm objective aperture. Data were collected in
558 super-resolution mode using a post-column quantum energy filter (Gatan) with a 20 eV slit and
559 K3 Gatan direct detector. Data were acquired using EPU2.7 with aberration-free image shift
560 (AFIS) and a defocus range of -0.8 to -2.4. The dataset was recorded using a pixel size of 0.651
561 Å/pixel (0.3225 Å/pixel in super-resolution mode) with a total exposure time of 1s (38 individual
562 frames) and a dose of 1.696 $e^-/Å^2$/frame. The total electron dose for the specimen was 61 $e^-/Å^2$ for
563 dataset 1 and 67 $e^-/Å^2$ for dataset 2.

564

565 **Cryo-EM data processing**

566 Cryo-EM data were processed using CryoSPARC v3.2.0-4.0 (Punjani, Rubinstein, Fleet, &
567 Brubaker, 2017) (Figure 2—figure supplement 1). All movies were subjected to motion correction
568 using patch motion correction . Following patch CTF estimation, high quality micrographs were
569 identified based on relative ice thickness, CTF resolution estimation and total full frame motion.
570 1,749,907 particles were picked following the generation of 2D templates for automated template
571 picking. Subsequently, picked particles were binned x2.4 using a box-size of 360 pixels for 2D
572 classification (pixel size 1.56 Å/pixel). Following three rounds of 2D classifications, particles were

573 selected based upon visual inspection. Classes were selected that displayed general structural
574 features characteristic for the SLC26 family in various orientations. From this, 256,581 particles
575 were used to generate a 'good' ab initio model and a portion of rejected particles (16,030 particles)
576 were used to generate a 'junk' class. 967,713 selected particles from 2D classification were
577 subjected to heterogenous refinement using the selected good models as a 'template' and the junk
578 model as a 'decoy' model. After several rounds of heterogenous refinement, the selected 507,174
579 particles and associated heterogeneously refined map were subjected to multiple rounds of non-
580 uniform refinement with imposed C2 symmetry. Following iterative rounds of non-uniform and
581 local CTF refinement a reconstruction of a nominal resolution at 3.55 Å was generated. These
582 particles were then subjected to a 4-class ab initio for further sorting resulting in one good map
583 comprised of 173,834 particles. Particles were re-extracted with a bin-1 pixel size of 0.651 Å/pixel
584 using 432 pixel-sized box and subjected to non-uniform refinement prior to a final 3-class ab initio
585 resulting in a single good map comprised of 93,169 particles. Multiple rounds of non-uniform
586 refinement and local CTF refinement were performed. Finally, the resultant reconstruction maps
587 were sharpened with the DeepEMhancer tool using the HighRes deep-learning model (Sanchez-
588 Garcia et al., 2021). The quality of the map was evaluated and evaluated using 3DFSC (Tan et al.,
589 2017) for FSC validation and local resolution estimation.
590

591 **Cryo-EM model building and refinement**

592 Map interpretation was performed in Coot (Emsley & Cowtan, 2004) using a model of SLC26A6
593 obtained from the AlphaFold Protein Structure Database (Jumper et al., 2021; Varadi et al., 2022)
594 as template. The quality of the map allowed for the unambiguous assignment of residues 28-49,
595 62-594 and 655-747. The model was iteratively improved by real space refinement in PHENIX

596 (Afonine et al., 2018) maintaining NCS and secondary structure constrains throughout. Figures
597 were generated using ChimeraX (Pettersen et al., 2004) and Dino (http://www.dino3d.org).
598 Surfaces were generated with MSMS (Sanner, Olson, & Spehner, 1996).
599

600 **Data availability**

601 The cryo-EM density map of hSLC26A6 has been deposited in the Electron Microscopy Data
602 Bank under ID code XXX. The coordinates for the atomic model of hSLC26A6 has been deposited
603 in the Protein Data Bank under ID code YYY. Transport experiments are provided as source data.

604

605 **Author Contributions**

606 D.N.T has cloned, expressed and purified proteins, carried out electrophysiology and transport
607 experiments, prepared samples for cryo-EM, processed cryo-EM data and built models. M.S.
608 assisted in cryo-EM data collection and processing. C.B. and S.J.B. synthesized probe used for
609 HCO_3^- transport experiments. D.N.T and R.D. jointly planned experiments and wrote the
610 manuscript with input from all authors.

611

612 **Author Information**

613 The authors declare no competing financial interests. Correspondence and requests for materials
614 should be addressed to R.D. (dutzler@bioc.uzh.ch).
615

616 **Acknowledgments** We thank the Center for Microscopy and Image Analysis (ZMB) of the
617 University of Zurich for the support and access to the electron microscopes. All members of the

618 Dutzler lab are acknowledged for their help at various stages of the project. We thank Anastasiia
619 Sukalskia, Elena Lehmann, Katarzyna Drozdzyk and Melanie Arndt for their help in cryo-EM data
620 acquisition. Justin Walter is acknowledged for the cloning of initial constructs and advice in the
621 SLC26 project. This research was supported by a grant from the Swiss National Science
622 Foundation (No. 31003A_163421) to R.D. SJB acknowledges the Engineering and Physical
623 Sciences Research Council (EPSRC) for funding [EP/S032339/1].

624

625 **References**

626 Afonine, P. V., Poon, B. K., Read, R. J., Sobolev, O. V., Terwilliger, T. C., Urzhumtsev, A., &
627 Adams, P. D. (2018). Real-space refinement in PHENIX for cryo-EM and crystallography.
628 *Acta Crystallogr D Struct Biol, 74*(Pt 6), 531-544. doi:10.1107/S2059798318006551
629 Alka, K., & Casey, J. R. (2014). Bicarbonate transport in health and disease. *IUBMB Life, 66*(9),
630 596-615. doi:10.1002/iub.1315
631 Alper, S. L., & Sharma, A. K. (2013). The SLC26 gene family of anion transporters and channels.
632 *Mol Aspects Med, 34*(2-3), 494-515. doi:10.1016/j.mam.2012.07.009
633 Bavi, N., Clark, M. D., Contreras, G. F., Shen, R., Reddy, B. G., Milewski, W., & Perozo, E.
634 (2021). The conformational cycle of prestin underlies outer-hair cell electromotility.
635 *Nature, 600*(7889), 553-558. doi:10.1038/s41586-021-04152-4
636 Bertrand, C. A., Mitra, S., Mishra, S. K., Wang, X., Zhao, Y., Pilewski, J. M., . . . Frizzell, R. A.
637 (2017). The CFTR trafficking mutation F508del inhibits the constitutive activity of
638 SLC26A9. *Am J Physiol Lung Cell Mol Physiol, 312*(6), L912-L925.
639 doi:10.1152/ajplung.00178.2016

640 Butan, C., Song, Q., Bai, J. P., Tan, W. J. T., Navaratnam, D., & Santos-Sacchi, J. (2022). Single
641 particle cryo-EM structure of the outer hair cell motor protein prestin. *Nat Commun, 13*(1),
642 290. doi:10.1038/s41467-021-27915-z
643 Chernova, M. N., Jiang, L., Friedman, D. J., Darman, R. B., Lohi, H., Kere, J., . . . Alper, S. L.
644 (2005). Functional comparison of mouse slc26a6 anion exchanger with human SLC26A6
645 polypeptide variants: differences in anion selectivity, regulation, and electrogenicity. *J Biol*
646 *Chem, 280*(9), 8564-8580. doi:10.1074/jbc.M411703200
647 Chi, X., Jin, X., Chen, Y., Lu, X., Tu, X., Li, X., . . . Pan, X. (2020). Structural insights into the
648 gating mechanism of human SLC26A9 mediated by its C-terminal sequence. *Cell Discov,*
649 *6*, 55. doi:10.1038/s41421-020-00193-7
650 Clark, J. S., Vandorpe, D. H., Chernova, M. N., Heneghan, J. F., Stewart, A. K., & Alper, S. L.
651 (2008). Species differences in Cl- affinity and in electrogenicity of SLC26A6-mediated
652 oxalate/Cl- exchange correlate with the distinct human and mouse susceptibilities to
653 nephrolithiasis. *J Physiol, 586*(5), 1291-1306. doi:10.1113/jphysiol.2007.143222
654 Dorwart, M. R., Shcheynikov, N., Wang, Y., Stippec, S., & Muallem, S. (2007). SLC26A9 is a
655 Cl(-) channel regulated by the WNK kinases. *J Physiol, 584*(Pt 1), 333-345.
656 doi:10.1113/jphysiol.2007.135855
657 Dorwart, M. R., Shcheynikov, N., Yang, D., & Muallem, S. (2008). The solute carrier 26 family
658 of proteins in epithelial ion transport. *Physiology (Bethesda), 23*, 104-114.
659 doi:10.1152/physiol.00037.2007
660 Drew, D., & Boudker, O. (2016). Shared Molecular Mechanisms of Membrane Transporters. *Annu*
661 *Rev Biochem, 85*, 543-572. doi:10.1146/annurev-biochem-060815-014520

Emsley, P., & Cowtan, K. (2004). Coot: model-building tools for molecular graphics. *Acta Crystallogr D Biol Crystallogr, 60*(Pt 12 Pt 1), 2126-2132. doi:S0907444904019158 [pii] 10.1107/S0907444904019158

Futamata, H., Fukuda, M., Umeda, R., Yamashita, K., Tomita, A., Takahashi, S., . . . Nureki, O. (2022). Cryo-EM structures of thermostabilized prestin provide mechanistic insights underlying outer hair cell electromotility. *Nat Commun, 13*(1), 6208. doi:10.1038/s41467-022-34017-x

Ge, J., Elferich, J., Dehghani-Ghahnaviyeh, S., Zhao, Z., Meadows, M., von Gersdorff, H., . . . Gouaux, E. (2021). Molecular mechanism of prestin electromotive signal amplification. *Cell, 184*(18), 4669-4679 e4613. doi:10.1016/j.cell.2021.07.034

Geertsma, E. R., Chang, Y. N., Shaik, F. R., Neldner, Y., Pardon, E., Steyaert, J., & Dutzler, R. (2015). Structure of a prokaryotic fumarate transporter reveals the architecture of the SLC26 family. *Nat Struct Mol Biol, 22*(10), 803-808. doi:10.1038/nsmb.3091

Geertsma, E. R., & Dutzler, R. (2011). A versatile and efficient high-throughput cloning tool for structural biology. *Biochemistry, 50*(15), 3272-3278. doi:10.1021/bi200178z

Jiang, Z., Asplin, J. R., Evan, A. P., Rajendran, V. M., Velazquez, H., Nottoli, T. P., . . . Aronson, P. S. (2006). Calcium oxalate urolithiasis in mice lacking anion transporter Slc26a6. *Nat Genet, 38*(4), 474-478. doi:10.1038/ng1762

Jumper, J., Evans, R., Pritzel, A., Green, T., Figurnov, M., Ronneberger, O., . . . Hassabis, D. (2021). Highly accurate protein structure prediction with AlphaFold. *Nature, 596*(7873), 583-589. doi:10.1038/s41586-021-03819-2

683 Kim, H. J., Myers, R., Sihn, C. R., Rafizadeh, S., & Zhang, X. D. (2013). Slc26a6 functions as an
684 electrogenic Cl-/HCO3- exchanger in cardiac myocytes. *Cardiovasc Res, 100*(3), 383-391.
685 doi:10.1093/cvr/cvt195
686 Knauf, F., Yang, C. L., Thomson, R. B., Mentone, S. A., Giebisch, G., & Aronson, P. S. (2001).
687 Identification of a chloride-formate exchanger expressed on the brush border membrane of
688 renal proximal tubule cells. *Proc Natl Acad Sci U S A, 98*(16), 9425-9430.
689 doi:10.1073/pnas.141241098
690 Liu, Q., Zhang, X., Huang, H., Chen, Y., Wang, F., Hao, A., . . . Chen, Z. (2022). Asymmetric
691 Pendrin Homodimer Reveals its Molecular Mechanism as Anion Exchanger. *bioRxiv*,
692 2022.2001.2014.476289. doi:10.1101/2022.01.14.476289
693 Lohi, H., Kujala, M., Kerkela, E., Saarialho-Kere, U., Kestila, M., & Kere, J. (2000). Mapping of
694 five new putative anion transporter genes in human and characterization of SLC26A6, a
695 candidate gene for pancreatic anion exchanger. *Genomics, 70*(1), 102-112.
696 doi:10.1006/geno.2000.6355
697 Lu, F., Li, S., Jiang, Y., Jiang, J., Fan, H., Lu, G., . . . Yan, N. (2011). Structure and mechanism of
698 the uracil transporter UraA. *Nature, 472*(7342), 243-246. doi:10.1038/nature09885
699 Martínez-Crespo, L., Hewitt, S. H., De Simone, N. A., Šindelář, V., Davis, A. P., Butler, S., &
700 Valkenier, H. (2021). Transmembrane Transport of Bicarbonate Unravelled**. *Chemistry*
701 *– A European Journal, 27*(26), 7367-7375. doi:https://doi.org/10.1002/chem.202100491
702 Ohana, E., Shcheynikov, N., Moe, O. W., & Muallem, S. (2013). SLC26A6 and NaDC-1
703 transporters interact to regulate oxalate and citrate homeostasis. *J Am Soc Nephrol, 24*(10),
704 1617-1626. doi:10.1681/ASN.2013010080

705 Ohana, E., Yang, D., Shcheynikov, N., & Muallem, S. (2009). Diverse transport modes by the
706 solute carrier 26 family of anion transporters. *J Physiol, 587*(Pt 10), 2179-2185.
707 doi:10.1113/jphysiol.2008.164863
708 Pettersen, E. F., Goddard, T. D., Huang, C. C., Couch, G. S., Greenblatt, D. M., Meng, E. C., &
709 Ferrin, T. E. (2004). UCSF Chimera--a visualization system for exploratory research and
710 analysis. *J Comput Chem, 25*(13), 1605-1612. doi:10.1002/jcc.20084
711 Sanner, M. F., Olson, A. J., & Spehner, J. C. (1996). Reduced surface: an efficient way to compute
712 molecular surfaces. *Biopolymers, 38*(3), 305-320. doi:10.1002/(SICI)1097-
713 0282(199603)38:3<305::AID-BIP4>3.0.CO;2-Y
714 Shcheynikov, N., Ko, S. B., Zeng, W., Choi, J. Y., Dorwart, M. R., Thomas, P. J., & Muallem, S.
715 (2006). Regulatory interaction between CFTR and the SLC26 transporters. *Novartis Found*
716 *Symp, 273*, 177-186; discussion 186-192, 261-174. Retrieved from
717 https://www.ncbi.nlm.nih.gov/pubmed/17120768
718 Shcheynikov, N., Wang, Y., Park, M., Ko, S. B., Dorwart, M., Naruse, S., . . . Muallem, S. (2006).
719 Coupling modes and stoichiometry of Cl-/HCO3- exchange by slc26a3 and slc26a6. *J Gen*
720 *Physiol, 127*(5), 511-524. doi:10.1085/jgp.200509392
721 Smart, O. S., Neduvelil, J. G., Wang, X., Wallace, B. A., & Sansom, M. S. (1996). HOLE: a
722 program for the analysis of the pore dimensions of ion channel structural models. *J Mol*
723 *Graph, 14*(6), 354-360, 376. Retrieved from
724 http://www.ncbi.nlm.nih.gov/pubmed/9195488
725 Varadi, M., Anyango, S., Deshpande, M., Nair, S., Natassia, C., Yordanova, G., . . . Velankar, S.
726 (2022). AlphaFold Protein Structure Database: massively expanding the structural

727 coverage of protein-sequence space with high-accuracy models. *Nucleic Acids Res, 50*(D1), D439-D444. doi:10.1093/nar/gkab1061

729 Walter, J. D., Sawicka, M., & Dutzler, R. (2019). Cryo-EM structures and functional characterization of murine Slc26a9 reveal mechanism of uncoupled chloride transport. *Elife, 8*. doi:10.7554/eLife.46986

732 Wang, C., Sun, B., Zhang, X., Huang, X., Zhang, M., Guo, H., . . . Zhang, P. (2019). Structural mechanism of the active bicarbonate transporter from cyanobacteria. *Nat Plants, 5*(11), 1184-1193. doi:10.1038/s41477-019-0538-1

735 Wang, J., Wang, W., Wang, H., & Tuo, B. (2020). Physiological and Pathological Functions of SLC26A6. *Front Med (Lausanne), 7*, 618256. doi:10.3389/fmed.2020.618256

737 Wang, L., Chen, K., & Zhou, M. (2021). Structure and function of an Arabidopsis thaliana sulfate transporter. *Nat Commun, 12*(1), 4455. doi:10.1038/s41467-021-24778-2

739 Wang, Y., Soyombo, A. A., Shcheynikov, N., Zeng, W., Dorwart, M., Marino, C. R., . . . Muallem, S. (2006). Slc26a6 regulates CFTR activity in vivo to determine pancreatic duct HCO3- secretion: relevance to cystic fibrosis. *EMBO J, 25*(21), 5049-5057. doi:10.1038/sj.emboj.7601387

743 Xie, Q., Welch, R., Mercado, A., Romero, M. F., & Mount, D. B. (2002). Molecular characterization of the murine Slc26a6 anion exchanger: functional comparison with Slc26a1. *Am J Physiol Renal Physiol, 283*(4), F826-838. doi:10.1152/ajprenal.00079.2002

746 Zheng, J., Shen, W. X., He, D. Z. Z., Kevin, B. L., Madison, L. D., & Dallos, P. (2000). Prestin is the motor protein of cochlear outer hair cells. *Nature, 405*(6783), 149-155. doi:Doi 10.1038/35012009

749 **Figures**

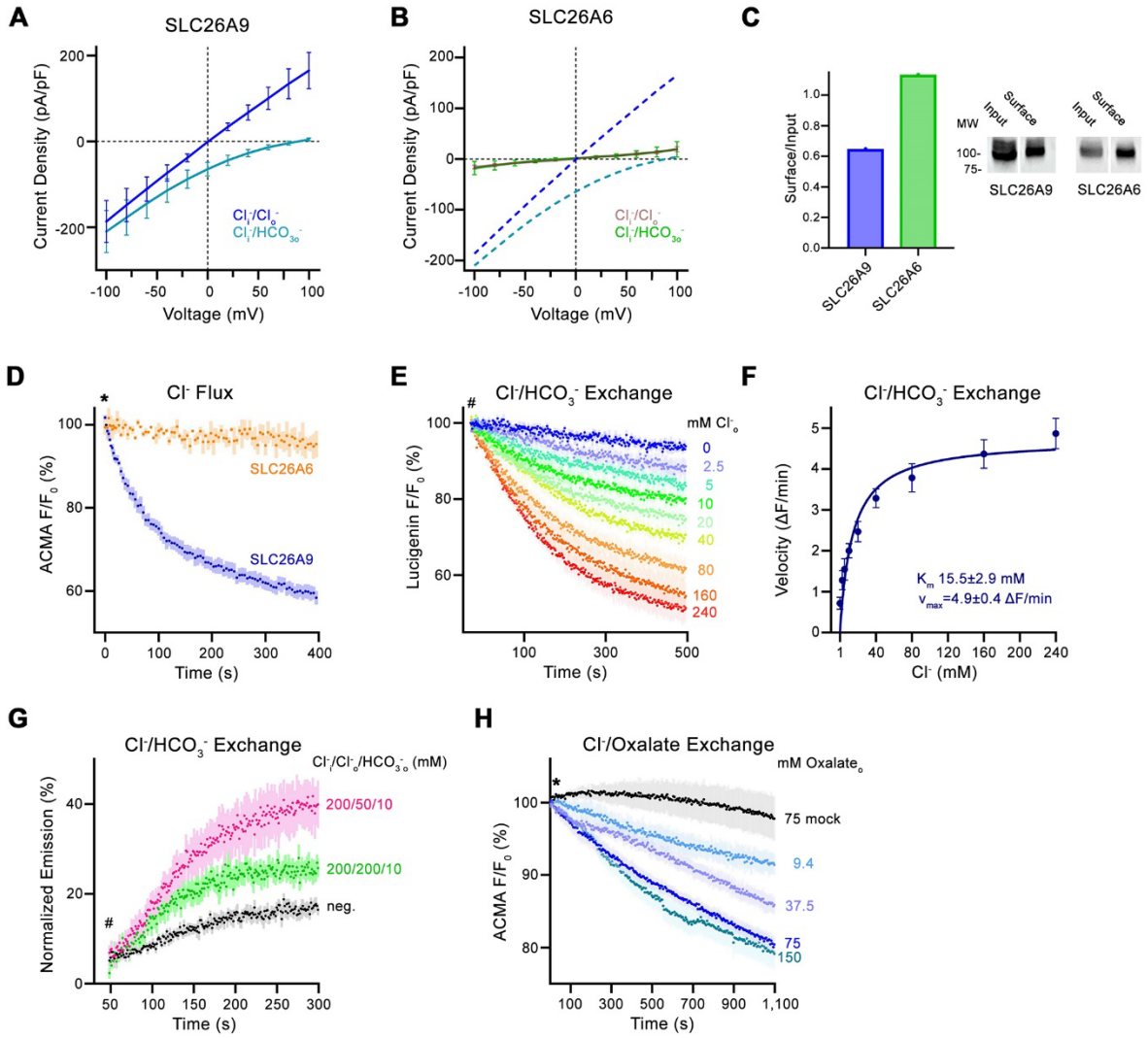

750

751 **Figure 1.** Transport properties of SLC26A6. (**A**) Current-Voltage relationships of HEK 293 cells
752 expressing the protein SLC26A9 and (**B**) SLC26A6. Data were recorded in the whole-cell
753 configuration in symmetric (150 mM) Cl^- concentrations and asymmetric conditions with
754 equimolar (150 mM) concentrations of intracellular Cl^- and extracellular HCO_3^-. Values show
755 mean of independent experiments (SLC26A9 Cl^-/Cl^- n=6, Cl^-/ HCO_3^-, n=6; SLC26A6 Cl^-/Cl^- n=6,
756 Cl^-/ HCO_3^-, n=6). Dashed lines in (**B**) correspond to SLC26A9 data displayed in (**A**). (**C**) Protein

757 expression at the surface of HEK cells determined by surface biotinylation. Ratio of biotinylated
758 over total protein (left) as quantified from a Western blot against myc-tag fused to the C-terminus
759 of the respective constructs. (**D**) Uncoupled Cl^- transport mediated by either SLC26A9 or
760 SLC26A6 reconstituted into proteoliposomes, as monitored by the fluorescence change of the pH
761 gradient-sensitive fluorophore ACMA. Traces show mean of 7 and 3 replicates from 2 independent
762 reconstitutions for SLC26A9 and SLC26A6. (**E**) Coupled Cl^-/HCO_3^- exchange monitored by the
763 time and Cl^- concentration dependent quenching of the fluorophore lucigenin trapped inside
764 proteoliposomes. Traces show mean of 6 independent experiments form 3 reconstitutions. (**F**) Cl^-
765 concentration dependence of transport. Initial velocities were obtained from individual
766 measurements displayed in (**E**), the solid line shows a fit to the Michaelis Menten equation with
767 an apparent K_m of 16 mM. (**G**) Coupled Cl^-/HCO_3^- exchange monitored by the time and
768 Cl^- concentration dependent fluorescence increase of the fluorophore [$Eu.L1^+$] trapped inside
769 proteoliposomes. Traces show mean of 5 independent experiments from 3 reconstitutions. 'neg.'
770 refers to liposomes not containing SLC26A6. (**E, G**), Hashtag indicates addition of the assayed
771 anion. (**H**) Electrogenic Cl^-/oxalate exchange followed by the fluorescence change of the pH
772 gradient sensitive fluorophore ACMA. Traces show mean quenching of ACMA fluorescence in a
773 concentration-dependent manner for 75mM Mock (n = 5), 9.4mM SLC26A6 (n = 3), 37.5mM
774 SLC26A6 (n = 5), 75mM SLC26A6 (n = 6), 150mM SLC26A6 (n = 8) liposomes (from 2
775 reconstitutions. Mock refers to liposomes not containing SLC26A6. (**D**, **H**), Asterisk indicates
776 addition of the H^+ ionophore CCCP, which allows counterion movement and electrogenic Cl^-
777 transport to proceed. (**A**, **B**, **D-H**), errors are s.e.m..
778 The following figure supplements are available for figure 1:
779 **Figure supplement 1.** Transport data.

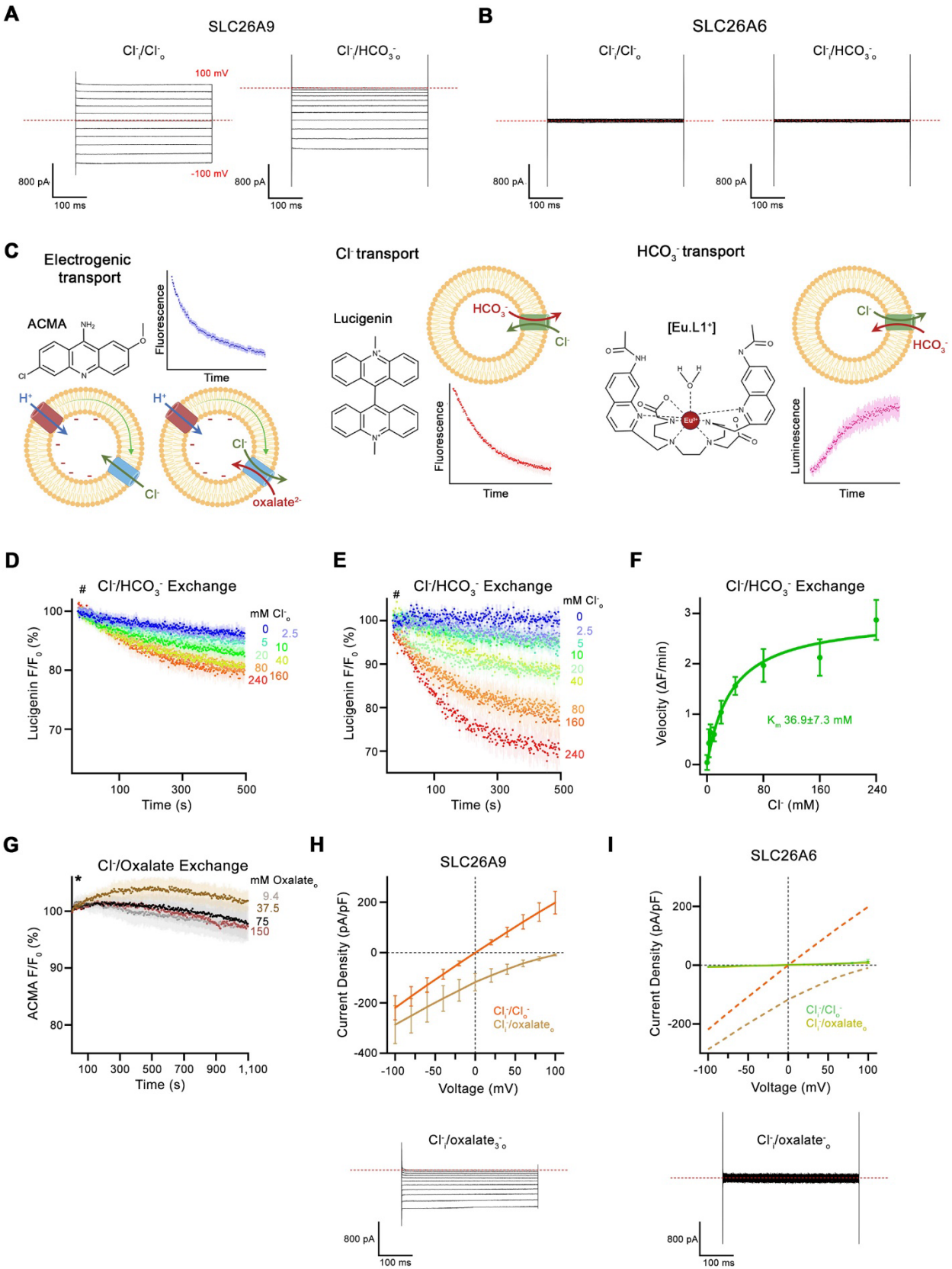
A
SLC26A9
Cl-i/Cl-o
Cl-i/HCO3-o
100 mV
-100 mV
800 pA
100 ms
B
SLC26A6
Cl-i/Cl-o
Cl-i/HCO3-o
800 pA
100 ms
C
Electrogenic transport
ACMA
Fluorescence
Time
H+
Cl-
oxalate2-
Cl- transport
Lucigenin
HCO3-
Cl-
Fluorescence
Time
HCO3- transport
[Eu.L1+]
Cl-
HCO3-
Luminescence
Time
D
Cl-/HCO3- Exchange
mM Cl-o
0
2.5
5
10
20
40
80
160
240
Lucigenin F/F0 (%)
Time (s)
E
Cl-/HCO3- Exchange
mM Cl-o
Lucigenin F/F0 (%)
Time (s)
F
Cl-/HCO3- Exchange
Velocity (ΔF/min)
Km 36.9±7.3 mM
Cl- (mM)
G
Cl-/Oxalate Exchange
mM Oxalateo
9.4
37.5
75
150
ACMA F/F0 (%)
Time (s)
H
SLC26A9
Current Density (pA/pF)
Cli-/Clo-
Cli-/oxalateo
Voltage (mV)
Cl-i/oxalate3-o
800 pA
100 ms
I
SLC26A6
Current Density (pA/pF)
Cli-/Clo-
Cli-/oxalateo
Voltage (mV)
Cl-i/oxalate-o
800 pA
100 ms

780

781 **Figure 1—figure supplement 1.** Transport data. (**A**, **B**) Representative whole-cell recordings of
782 HEK293 cells expressing SLC26A9 (**A**) or SLC26A6 (**B**) recorded by a step protocol. (**C**)
783 Proteoliposome-based ion transport assays used in this study. Left, electrogenic uncoupled Cl^- flux
784 or coupled Cl^-/oxalate exchange assayed by the decrease of the fluorescence of the pH-sensitive
785 fluorophore ACMA that is caused by the associated influx of H^+ mediated by the protonophore
786 CCCP to dissipate the membrane potential. Center, electroneutral Cl^-/HCO_3^- exchange assayed by
787 the quenching of the Cl^- selective fluorophore Lucigenin as a consequence of the influx of Cl^-.
788 Right, Influx of HCO_3^- into proteoliposomes as a consequence of electroneutral Cl^-/HCO_3^-
789 exchange, assayed by the luminescence increase of the HCO_3^- selective probe [Eu.L1$^+$]. Shown
790 are chemical formulas of the respective probes, schemes of the direction of transport and example
791 traces of the measured signals. (**D**) Time and Cl^- concentration dependent quenching of the
792 fluorophore lucigenin trapped inside liposomes not containing any protein determining the non-
793 specific background for experiments displayed in Figure 1E. Data show average of 6 experiments.
794 (**E**) Background-subtracted traces of the quenching of lucigenin by Cl^- as a consequence of coupled
795 Cl^-/HCO_3^- exchange displayed in Figure 1E. Data show mean of 6 independent experiments from
796 2 reconstitutions. (**D**, **E**), Hashtag indicates addition of the assayed anion. (**F**) Cl^- concentration
797 dependence of transport. Initial velocities were obtained from background-corrected individual
798 measurements displayed in (**E**), the solid line shows a fit to the Michaelis Menten equation with
799 an apparent K_m of 37 mM. (**G**) Time and concentration-dependent change of the fluorescence of
800 the pH gradient sensitive fluorophore ACMA upon addition of indicated concentrations of oxalate
801 to the outside of liposomes not containing any protein. The traces serve as negative controls for
802 the experiments displayed in Figure 1H. Traces show mean of 4-5 independent experiments.
803 Asterisk indicates addition of CCCP. (**H**) Current-Voltage relationships of HEK 293 cells

804 expressing the protein SLC26a9 and (**I**) SLC26A6. Data were recorded in the whole-cell
805 configuration in symmetric (150 mM) Cl^- concentrations and asymmetric conditions with
806 equimolar (150 mM) concentrations of intracellular Cl^- and extracellular oxalate. Values show
807 mean of independent experiments (SLC26A9 Cl^-/Cl^- n=4, Cl^-/oxalate, n=4; SLC26A6 Cl^-/Cl^- n=3,
808 Cl^-/oxalate, n=4. Representative current traces recorded in asymmetric Cl-/oxalate conditions are
809 shown below. Dashed lines in (**I**) correspond to SLC26A9 data displayed in (**H**). (**A**, **B**, **H**, **I**) Red
810 dashed line in recordings indicates 0 pA. (**D**-**I**), Errors are s.e.m..

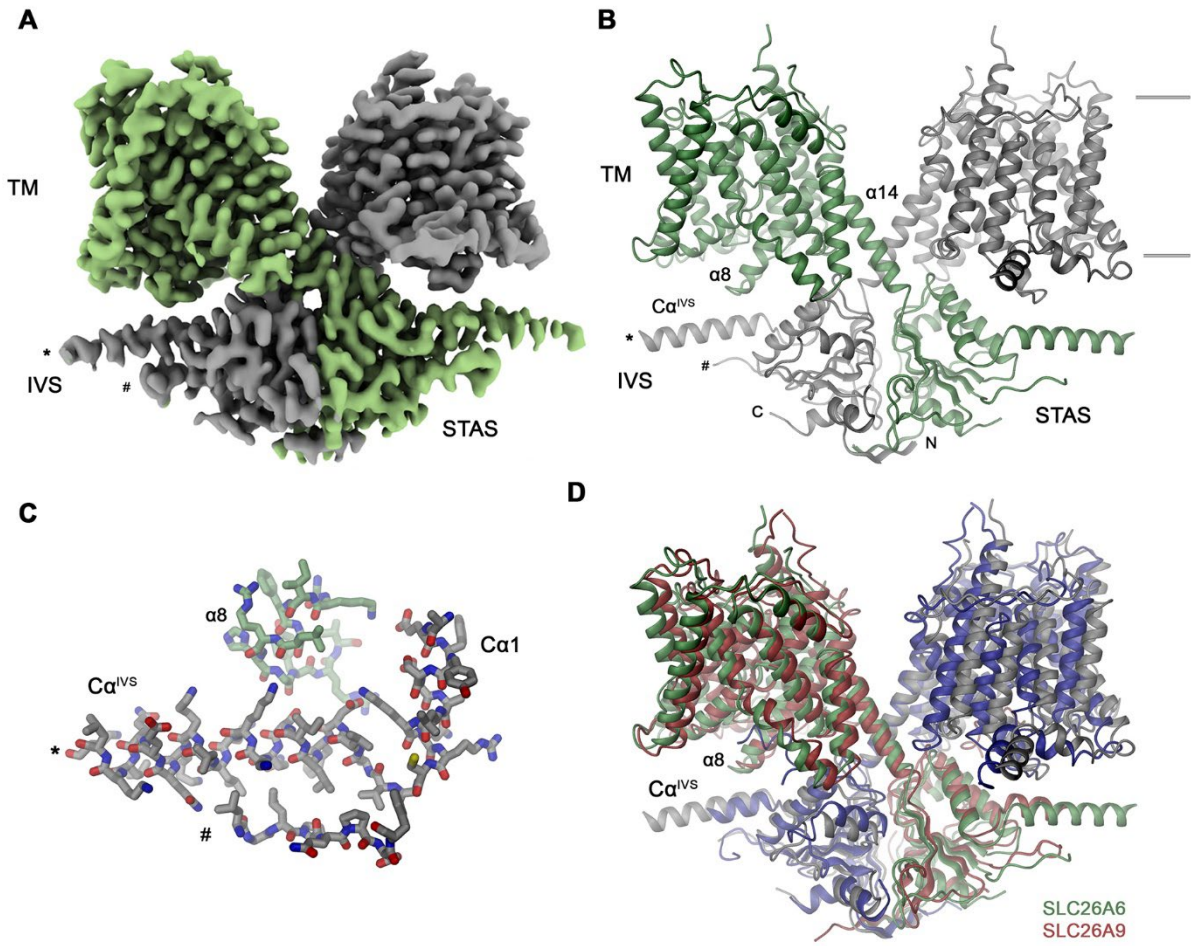

Figure 2. SLC26A6 structure. (**A**) Cryo-EM density of the SLC26A6 dimer at 3.28 Å and (**B**) ribbon representation of the model in the same orientation. Subunits are shown in unique colors and selected structural elements are labeled. The membrane boundary is indicated. (**C**) Interaction region between the loop proceeding α8 of the core domain and the helix $C\alpha^{IVS}$ of the adjacent subunit. (A-C) Start (*) and end (#) of the disordered region of the IVS are indicated. (D) Ribbon representation of the superimposed SLC26A6 (green, gray) and SLC26A9 (red, blue, PDBID: 7CH1) dimers.

The following figure supplements are available for figure 2:

Figure supplement 1. Cryo-EM reconstruction of SLC26A6.

821 **Figure supplement 2.** Section of the cryo-EM density of SLC26A6.

822 **Figure supplement 3.** Sequence and Topology.

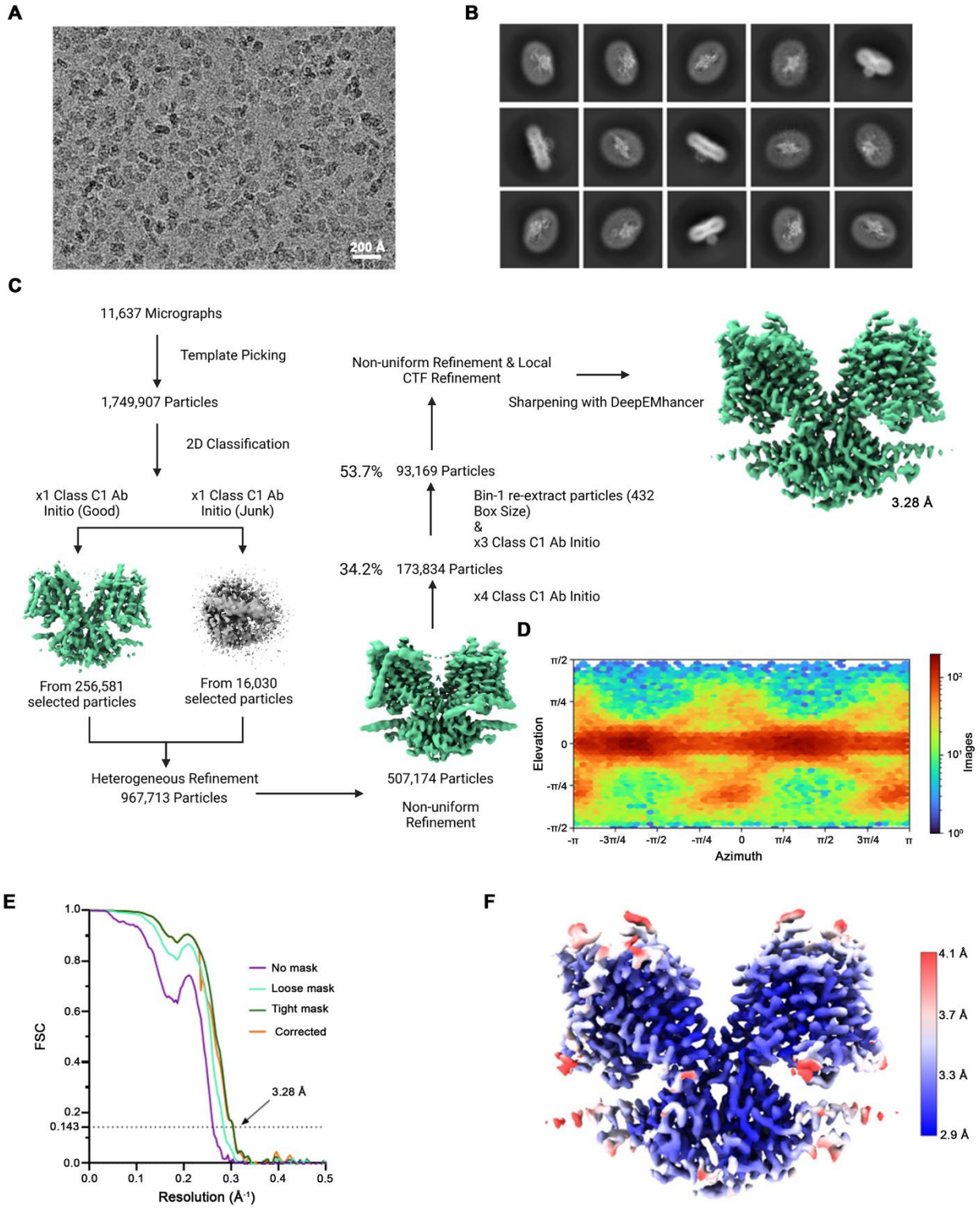

Figure 2—figure supplement 1. Cryo-EM reconstruction of SLC26A6. (**A**) Representative micrograph (of a total of 11,637) of the SLC26A6 dataset. (**B**) 2D class averages of SLC26A6.

826 (**C**) Data-processing workflow. Particles were extracted and subjected to 2D classification, and the
827 obtained 2D class averages were subsequently used as templates for particle picking. After
828 extraction, the new set of particles was subjected to a second round of 2D classification. Based on
829 2D class averages, particles were selected for an *ab initio* reconstructions A generated model
830 displaying protein features (green) and a 'decoy' model lacking such features (grey) were both
831 used for several rounds of heterogenous refinement, followed by non-uniform refinement.
832 Additional 2 multi-class *ab initio* reconstructions were performed for further sorting prior to non-
833 uniform refinement and local CTF refinement yielding a map at 3.28 Å resolution. (**D**) Heatmap
834 displaying the angular distribution of particle orientations. (**E**) FSC plot of cryo-EM density maps
835 of the SLC26A6 complex used for the estimation of its resolution. The dotted line indicates the
836 resolution at which the FSC drops below the 0.143 threshold. (**F**) Final 3D reconstruction colored
837 according to the local resolution.

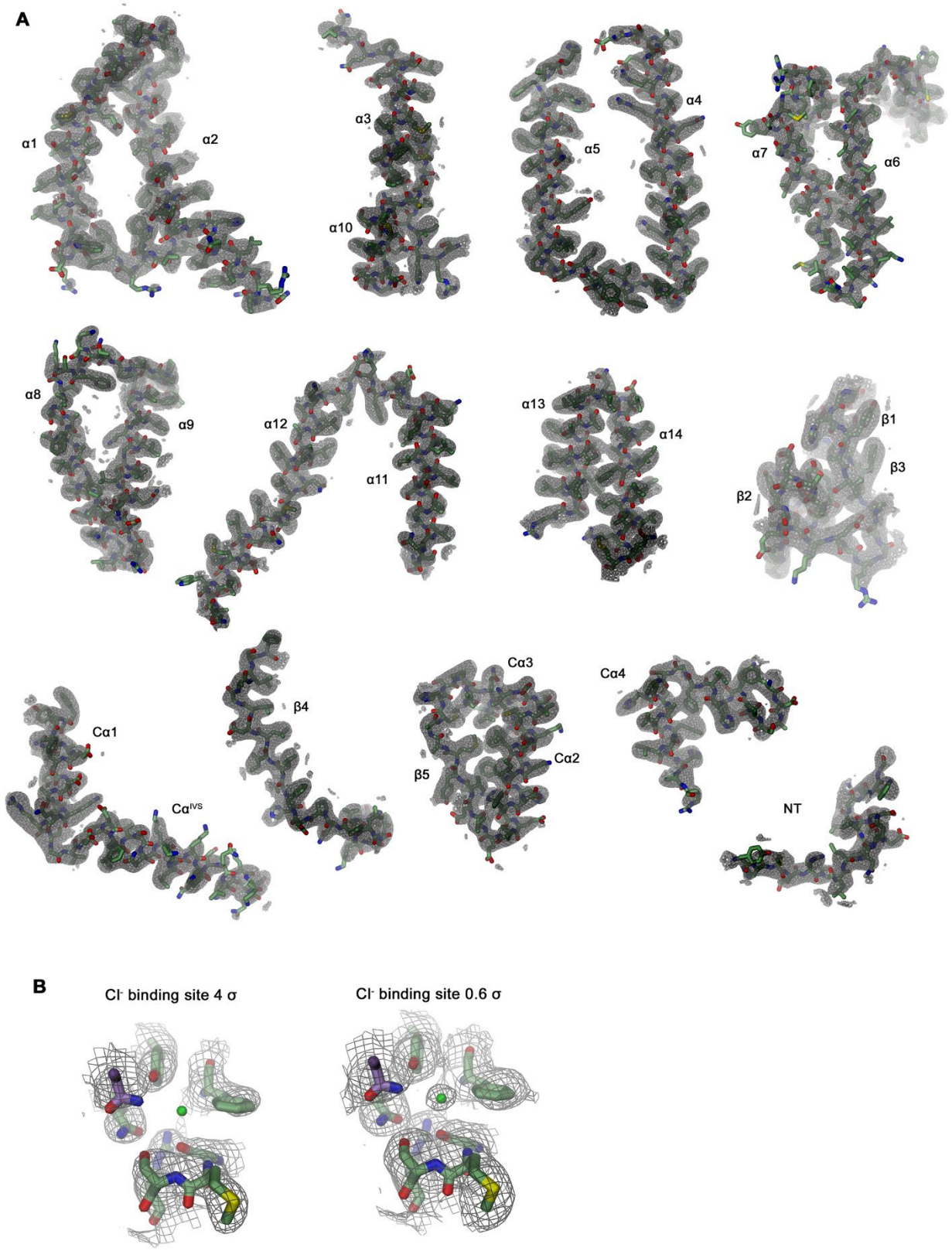
A
α1
α2
α3
α10
α4
α5
α7
α6
α8
α9
α12
α11
α13
α14
β1
β3
β2
Cα1
Cα^IVS
β4
Cα3
Cα2
β5
Cα4
NT
B
Cl⁻ binding site 4 σ
Cl⁻ binding site 0.6 σ

838

839 **Figure 2—figure supplement 2.** Section of the cryo-EM density of SLC26A6. (**A**) Cryo-EM
840 density at 3.28 Å (contoured at 4σ) superimposed on indicated parts of the model. (**B**) Cryo-EM
841 density surrounding the ion binding site at high (4 σ, left) and low (0.6 σ, right) contour
842 surrounding displayed residues. Residual density at low contour defines the position of a bound
843 Cl^- ion (green sphere).

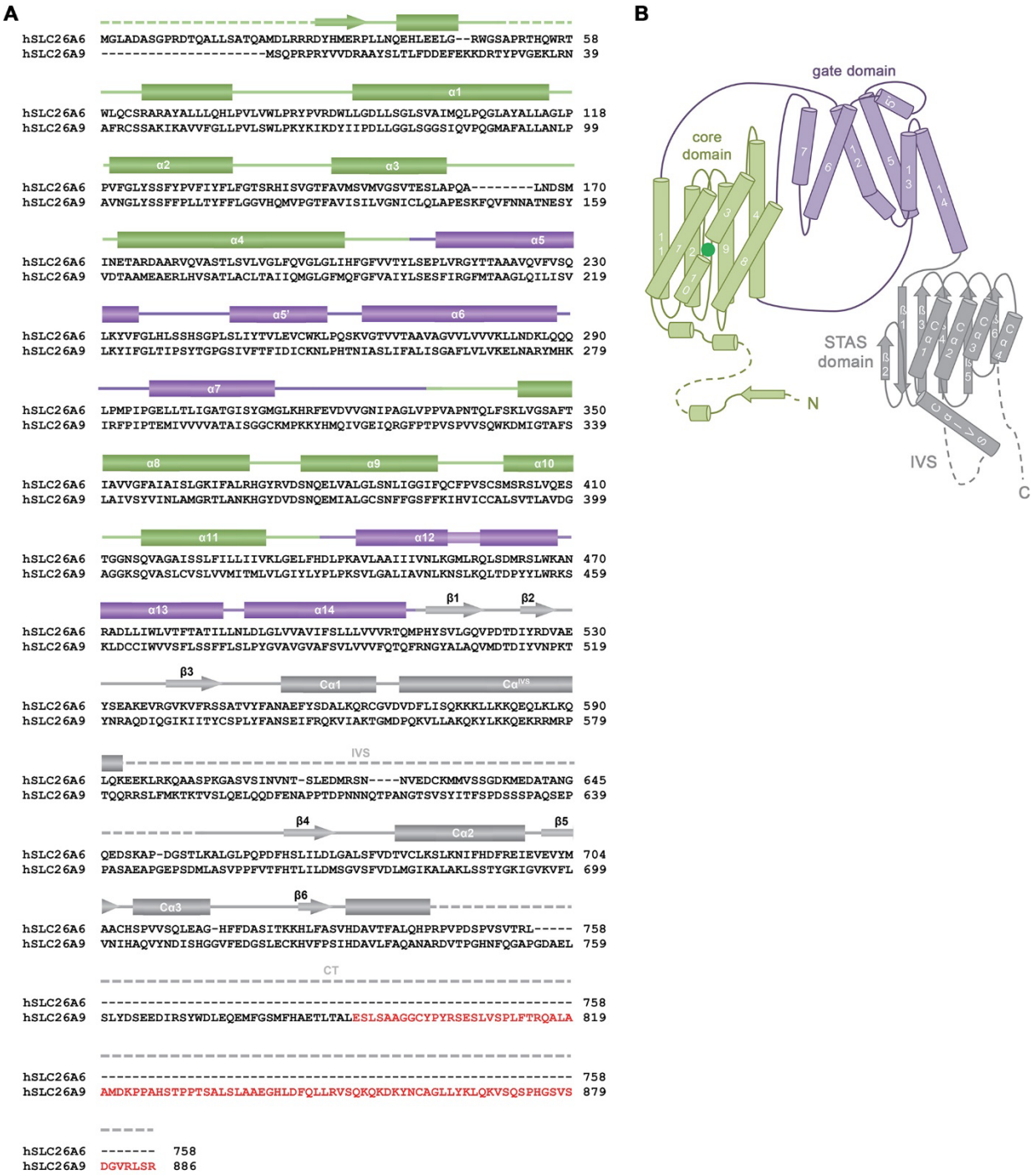

Figure 2—figure supplement 3. Sequence and Topology. (**A**) Sequence alignment of the human proteins SLC26A6 (isoform 3, NCBI reference sequence: NP_602298.2) and SLC26A9 (isoform b, NCBI reference sequence: NP_599152.2). Secondary structure elements of SLC26A6 are

848 indicated above, regions not defined in the structure are shown as dashed lines. An extension at
849 the C-terminus of SLC26A9 of isoform b compared to isoform a, which was shown to bind to the
850 cavity leading to the anion binding site in the inward-facing conformation of the transporter
851 (PDBID: 7CH1) is highlighted in red. (**B**) Topology of the SLC26A6 subunit. The different
852 domains of the transporter are indicated.

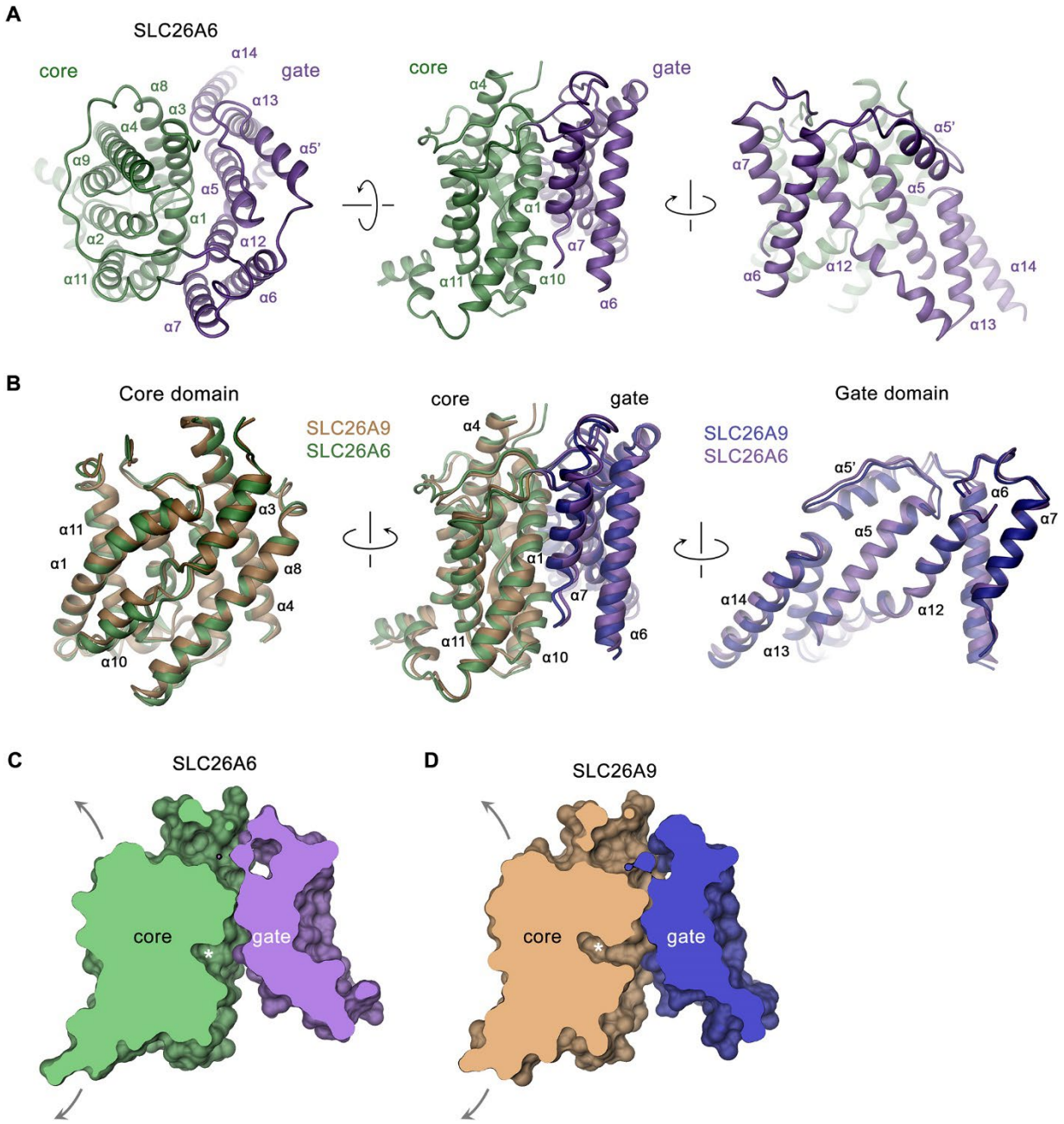

853

854 **Figure 3.** SLC26A6 TM domain. (**A**) Ribbon representation of the TM unit of SLC26A6 in
855 indicated orientations (left, view is from the outside, center and right, from within the membrane).
856 Core and gate domains are colored in green and violet, respectively. Selected secondary structure
857 elements are labeled. (**B**) Superposition of elements of the TM between SLC26A6 and SLC26A9
858 (PDBID: 7CH1). Left, core domains, center, TMs, right, gate domains. Core and gate domains of

859 SLC26A9 are colored in orange and blue, respectively. The view is from within the membrane,
860 relative orientations are indicated. (**C**) Slice across a surface of the TM domains of SLC26A6 (left)
861 and SLC26A9 (right) viewed from within the membrane. The spacious aqueous cavity leading to
862 the ion binding site from the cytoplasm is evident. Asterisk indicated the position of the transported
863 ion. Arrows indicate possible movements of the core domain.

864 The following figure supplements are available for figure 3:

865 **Figure supplement 1.** TM domain features.

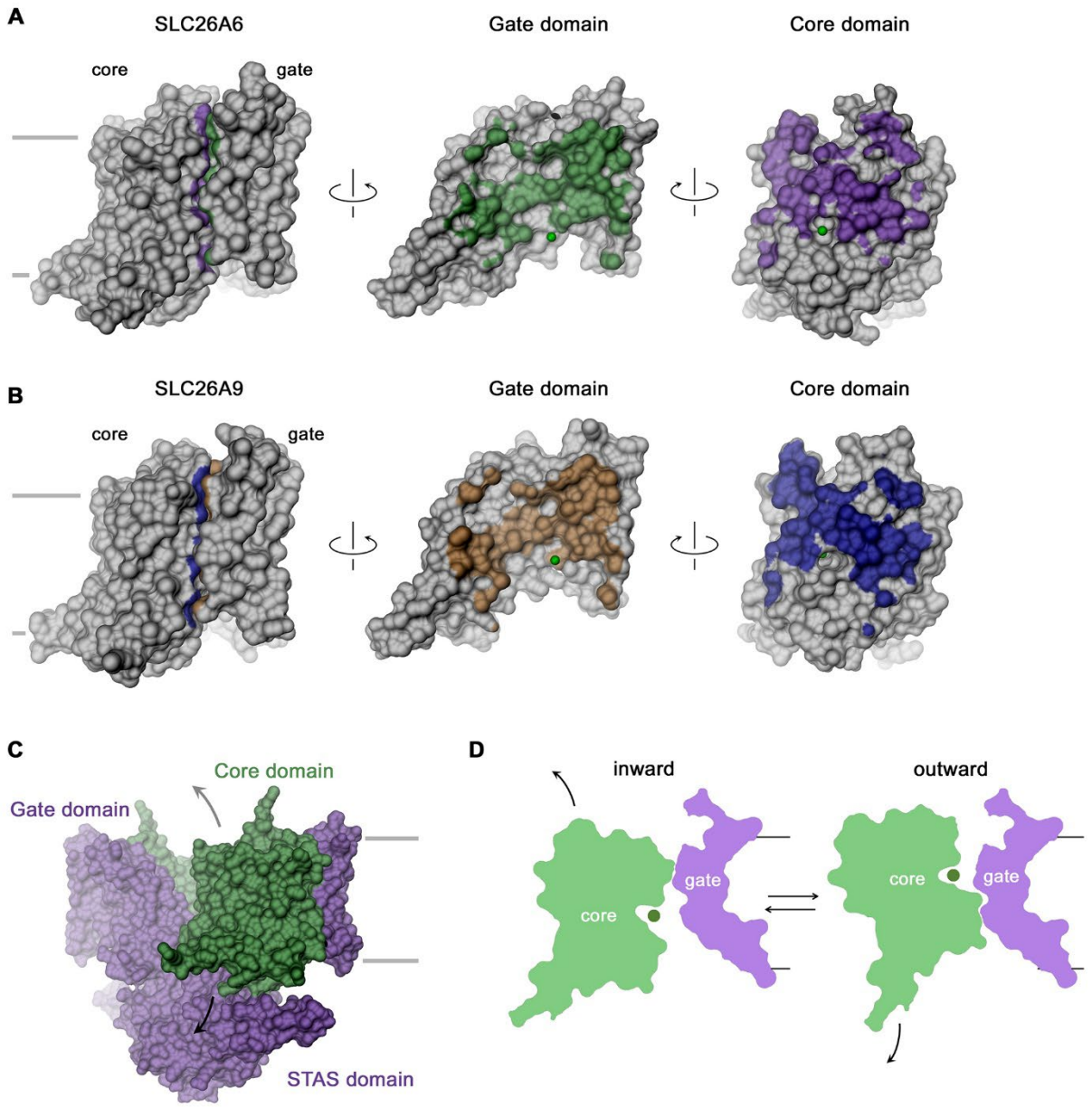

Figure 3—figure supplement 1. TM domain features. (**A**, **B**) Open book representation of the molecular surfaces of the TM (left) and its gate (center) and core domain (right) of SLC26A9 (**A**) and SLC26A6 (**B**). The coloring refers to the area contacted by the other domain. The position of the bound ion is indicated as green sphere. (**C**) Molecular surface of the SLC26A6 dimer with gate and STAS domains colored in violet and the core domains in green. (**D**) Schematic depiction of

872 slices across core and gate domains in the observed inward (left) and a hypothetic outward-facing
873 conformation (left). (**C**, **D**) Arrows indicate movements of the mobile core domain. (A-D)
874 Membrane boundaries are indicated.

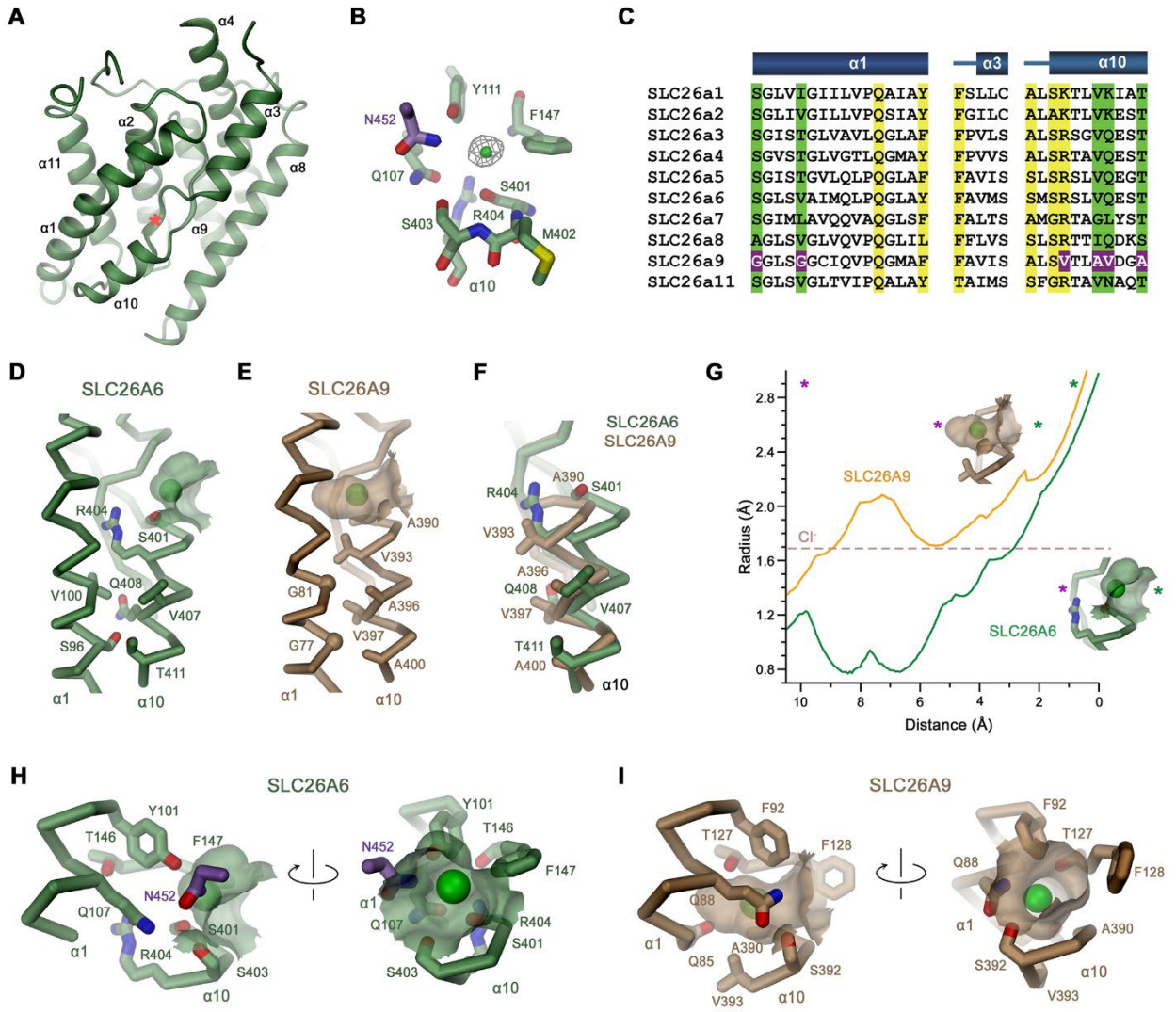

Figure 4. Features of the substrate binding site. (**A**) Ribbon representation of the core domain of SLC26A6 viewed from within the membrane from the gate domain. Asterisk indicates the location of the ion binding site, selected secondary structure elements are labeled. (**B**) Ion binding site with the density of a bound Cl- ion (green) displayed as mesh. (**C**) Sequence alignment of the ten functional human SLC26 paralogs in the region constituting the ion binding site. Conserved residues in the contact region between α1 and α10 are highlighted in green, residues involved in ion interactions in yellow. Deviating residues in SLC26A6 are highlighted in violet. Secondary structure elements are shown above. (**D**, **E**) Cα-representation of the contact region between α1

884 and α10 of (**D**) SLC26A6 and (**E**) SLC26A9 (PDBID: 7CH1). (**F**) α10 of both transporters
885 obtained from a superposition of the core domains. C-E sidechains of residues of the contact region
886 and selected residues of the binding site are shown as sticks. (**G**) Size of the substrate cavity of
887 SLC26A6 and SLC26A9 as calculated with HOLE (Smart, Neduvelil, Wang, Wallace, & Sansom,
888 1996). The radius of both proteins is mapped in the region between the two asterisks indicated in
889 the insets for either transporter. (**H**, **I**) Ion binding sites of SLC26A6 (**H**) and SLC26A9 (**I**). The
890 relative orientation of views is indicated. (**D**, **E**, **H**, **I**) The position of bound ions was inferred as
891 detailed in Figure supplement 1. The molecular surface surrounding the bound ions is displayed.
892 Sidechains of interacting residues are shown as sticks.

893 The following figure supplements are available for figure 4:

894 **Figure supplement 1.** Binding site comparisons.

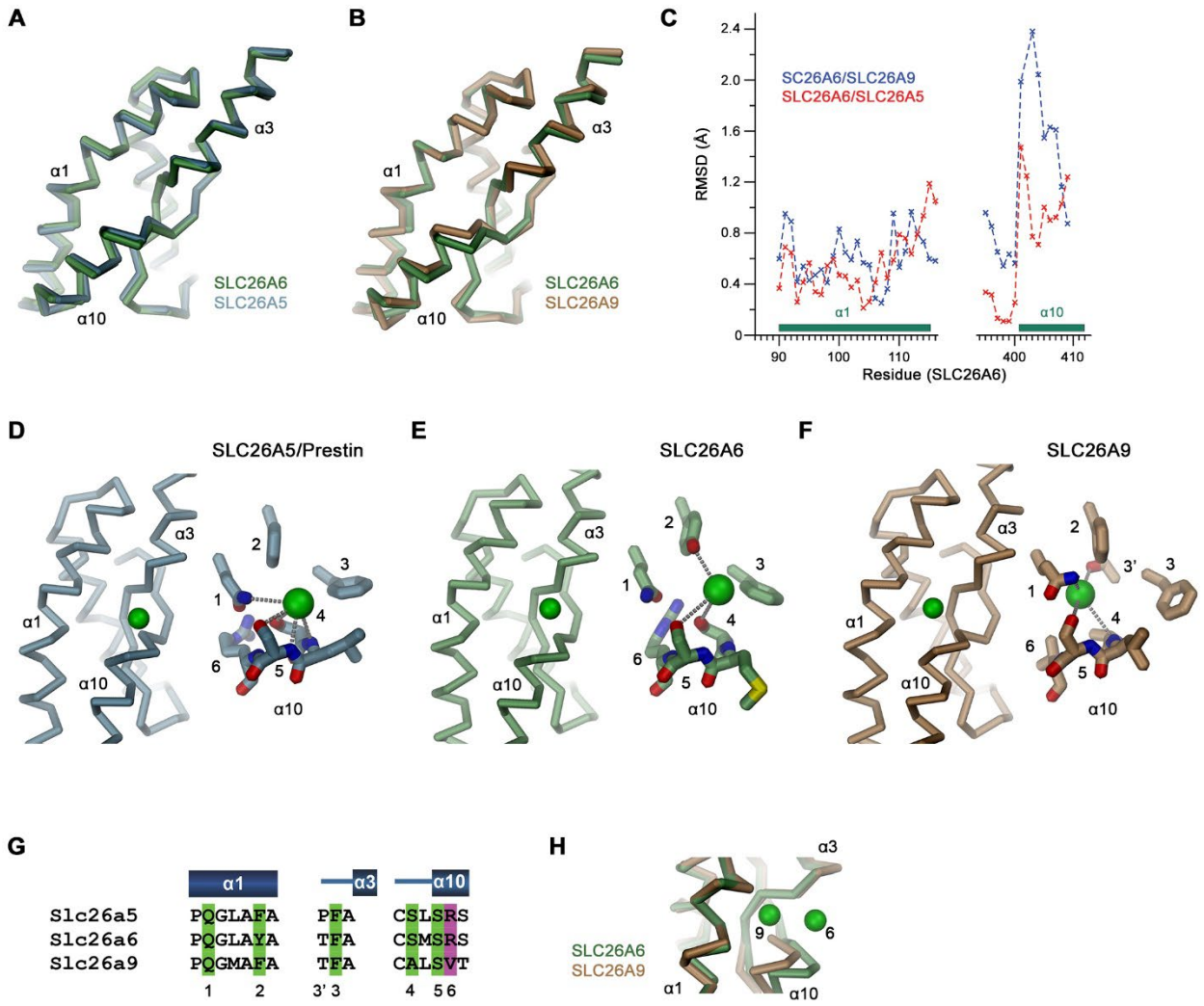

Figure 4—figure supplement 1. Binding site comparisons. (**A**, **B**) Superposition of secondary structure elements constituting the ion binding site of SLC26 transporters. (**A**) Comparison between SLC26A6 and SLC26A5 and (**B**) SLC26A9. (**C**) Positional difference between Cα-atoms in of the superpositions shown in (A, B). Whereas α1 is very similar in all three paralogs, the position of α10 differs between SLC26A6 and SLC26A9. (**D-F**) Ion interactions in (**D**) SLC26A5 (PDBID: 7LGU) and (**E)** SLC26A6 as defined in the respective datasets. (**F**) The Cl^- position in SLC26A9 was derived from residual density in the dataset of the map associated with PDBID 7CH1 (EMD-30368), which was assigned to a water molecule in the structure. (**D-F**) Shown is

904 the location of the ion in a Ca-trace of the binding site (left) and a close-up of the binding site with
905 presumable interactions to close-by groups indicated by dashed lines. (**G**) Alignment of residues
906 in the interaction region of the three paralogs. (**D**-**G**) Numbers refer to equivalent positions shown
907 in the alignment. (**H**) Difference in the position of a bound ion between SLC26A6 (6) and
908 SLC26A9 (9) obtained from a superposition of the binding regions.

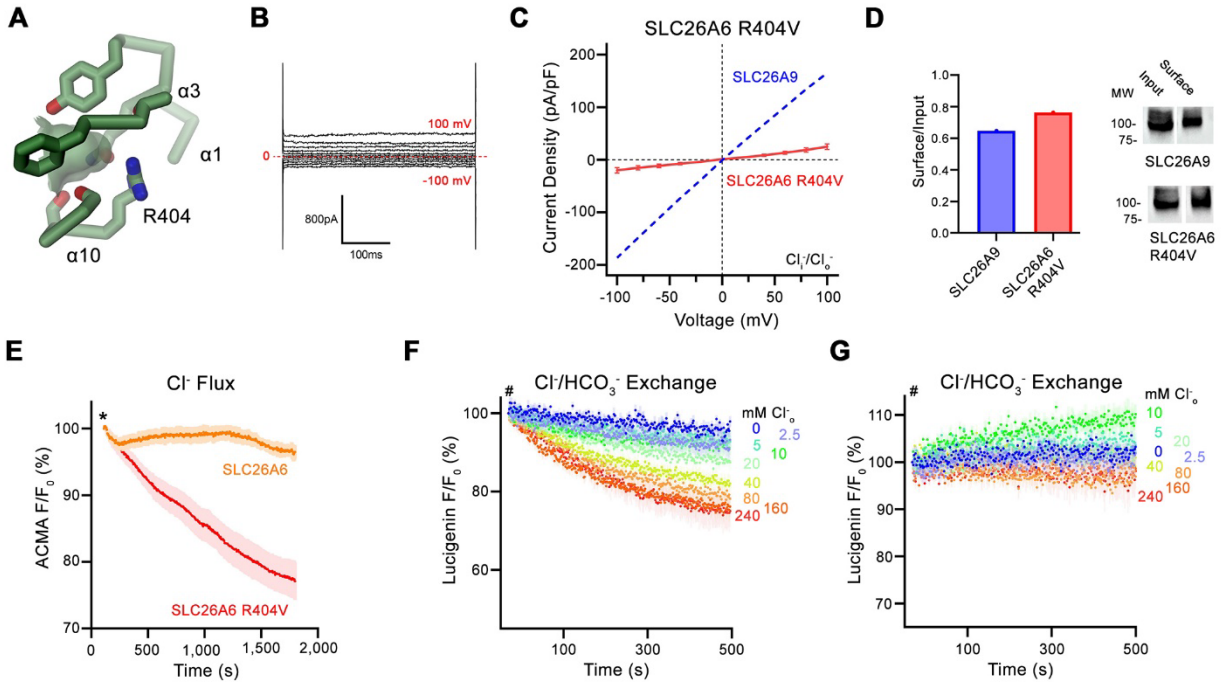

Figure 5. Functional properties of structure based SLC26A6 constructs. (**A**) SLC26 ion binding site showing surrounding residues including Arg 404. (**B**) Representative current trace and (**C**) current-voltage relationships of HEK 293 cells expressing the SLC26A6 mutation R404V. Data were recorded in the whole-cell configuration in symmetric (150 mM) Cl^- concentrations and asymmetric conditions with equimolar (150 mM) concentrations of intracellular Cl^- and extracellular HCO_3^-. Values show mean of 14 independent experiments. Dashed lines in correspond to SLC26A9 data displayed in Figure 1A. (**D**) Protein expression of SLC26A6 R404V and SLC26A9 at the surface of HEK cells determined by surface biotinylation. Ratio of biotinylated over total protein (left) as quantified from a Western blot against myc-tag fused to the C-terminus of the respective constructs. (**E**, **F**) Coupled Cl^-/HCO_3^- exchange by the SLC26A6 mutant R404V monitored by the time and Cl^- concentration dependent quenching of the fluorophore lucigenin trapped inside proteoliposomes. (**E**) Uncorrected traces and (**F**) traces corrected by the background obtained from empty liposomes displayed in Figure 1-figure

924 supplement 1C, which do not show indication of transport. (**E**, **F**) Traces show mean of a minimum

925 of 5 independent experiments form 2 reconstitutions. (**C**, **D**, **E**, **F**) errors are s.e.m..

926

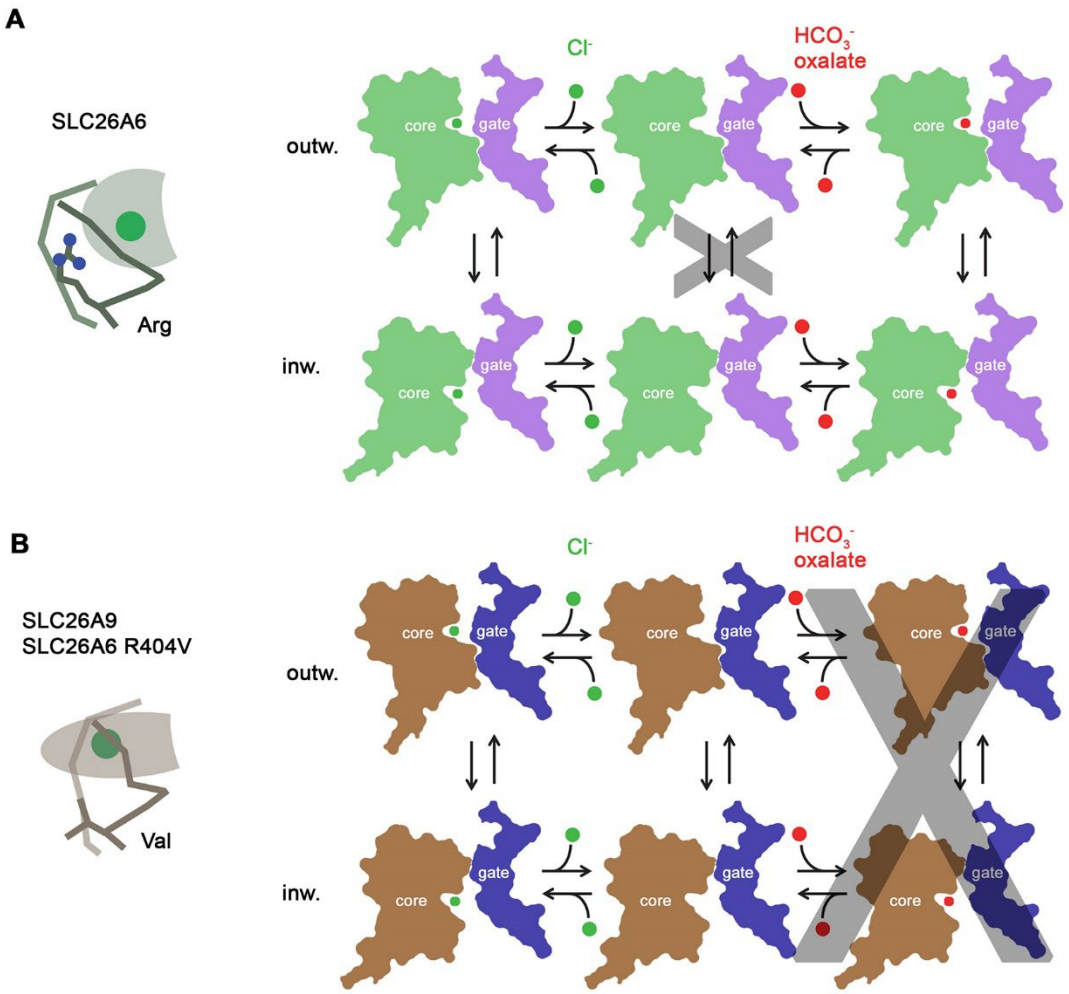

927

928 **Figure 6.** Transport mechanism. Features of the anion binding site (left) and kinetic schemes
929 (right) of two SLC26 paralogs with distinct functional properties. (**A**) The coupled antiporter
930 SLC26A6 mediates the strict stoichiometric exchange of Cl^- and either HCO_3^- or oxalate. The
931 protein readily cycles between inward- and outward-facing conformations in substrate-loaded
932 states, whereas the transition in an unloaded state is kinetically disfavored. The binding of different
933 anions is facilitated by a large but shallow binding site with high field-strength. (**B**) The uncoupled
934 Cl^- transporter SLC26A9 has a narrower substrate selectivity where both Cl^- and HCO_3^- are not
935 among the transported ions. Uncoupled Cl^- transport is likely mediated by a mechanism that allows
936 the rapid transition of the unloaded transporter between inward- and outward-facing

937 conformations. The transported ion binds to a site with low field-strength. A similar mechanism,
938 although with slower kinetics, is mediated by a point mutant of SLC26A6 where a conserved Arg
939 of the binding site is replaced by a Val, the corresponding residue found in SLC26A9.

940 **Table 1. Cryo-EM data collection, refinement and validation statistics.**

	hSLC26A6 in GDN (Combined data sets)	
Data collection and processing	**Data Set 1**	**Data Set 2**
Magnification	130,000	130,000
Voltage (kV)	300	300
Electron exposure (e–/Å^2)	61	67
Defocus range (μm)	−0.8 to −2.4	−1 to −2.4
Pixel size (Å)*	0.3255 (0.651)	0.3255 (0.651)
Symmetry imposed	C2	
Initial particle images (no.)	1,749,907	
Final particle images (no.)	93,169	
Map resolution (Å) FSC threshold 0.143	3.28	
Map resolution range (Å)	2.9-4.1	
Refinement		
Model resolution (Å) 0.5 FSC Threshold	3.3	
Model resolution range (Å)	1.5-3.3	
Map sharpening b-factor (Å^2)	121.9	
Model composition Non-hydrogen atoms Protein residues Ligands	 9994 1296 2	
B factors (Å^2) Protein Ligands	 120.71 30, 30	
R.m.s. deviations Bond lengths (Å) Bond angles (°)	 0.002 0.439	
Validation MolProbity score Clashscore Poor rotamers (%)	 1.90 6.29 2.73	
Ramachandran plot Favored (%) Allowed (%) Disallowed (%)	 96.57 3.43 0.0	

941